Development of Wideband Circularly Polarized Antennas Onboard Small Satellite for Ionospheric Observation and Communication

February 2020

Peberlin Parulian Sitompul

Graduate School of Science and Engineering

CHIBA UNIVERSITY

(千葉大学審査学位論文)

Development of Wideband Circularly Polarized Antennas Onboard Small Satellite for Ionospheric Observation and Communication

(小型衛星搭載の電離層観測及び通信用の広帯域円偏波アンテナの開発)

2020 年 2 月

Peberlin Parulian Sitompul

Graduate School of Science and Engineering

CHIBA UNIVERSITY

Declaration

I hereby declare that this submission is my oun work and that, to the best of my knowledge and belief, it contains no material which to a substansial extent has been accepted for the award of any other degree or diplomaof the university or other institute of higher learning, expect where due acknowledgment has been made in the text.

Peberlin Parulian Sitompul, February 2020

Abstract

Chiba University is developing the microsatellite which, makes use of the Electron Density -Temperature Probe (EDTP) sensors, the Global Navigation Satellite System (GNSS) Radio Occultation (RO) Receiver and Beacon Signal for Total Electron Content (TEC) measurement in Ionosphere layer of the Earth.

The objective of this research is to provide global coverage of the slant and vertical resolution of electron density in the ionosphere from 60-700 km from the Earth's surface. The electron density is essential to determine the quality of communication in high frequency (HF) radio communication, in satellite communication, and accuracy of global positioning. Nowadays, many researchers investigate the relationship between the electron density variation to global land deformation and earthquake events.

In this research, two novel methods are proposed to generate a circularly polarized (CP) signal and to enhance the axial ratio bandwidth (ARBW) based on the asymmetrical rectangular truncation and additional rectangular parasitic patch. This antenna will be used for the beacon transmitter in 2.2 GHz, bandwidth 40 MHz and, data communication in 2.5 GHz, bandwidth 100 MHz are proposed for small satellite or nanosatellite.

The first method introduces a pair of rectangular truncations and a shifted feed line to generate a circular polarization (CP) wave. The next step is to improve the 3-dB ARBW by attaching a rectangular-formed head on the feeding line. The designed antenna is fabricated to verify the simulated results. The measured antenna presents good agreement with the simulated one of 18.3% by achieving the ARBW of 14.9%.

The second method is the insertion of one parasitic patch to improve CP bandwidth and gain of an antenna. In this method, the linearly-polarized (LP) wave is converted to a circularly-polarized wave by truncating two

rectangular-formed slots, shifting the feeding line, and attaching a rectangular-shaped parasitic patch. The designed antenna is fabricated to verify the simulated results such as reflection coefficient, axial ratio bandwidth, gain. The measured result performs the 3-dB ARBW of 35.8% from 2.16-2.95 GHz and its reflection coefficient bandwidth of 47.3% from 1.77-2.81 GHz with peak gain 5 dBic at frequency 2.2 GHz. Thus, these designed antennas can be implemented for a small satellite, nanosatellite, and other applications that require a wideband circularly-polarized antenna, bidirectional pattern, and compact-designed structure.

抽象

電離層の電子密度情報は、高周波（HF）通信の安定性とグローバル位置情報の精度を向上させるために重要であり、さらに近年では、電離層の変動とグローバル地殻変動の関連性についての研究も多く行われている。千葉大学では現在、電離層における全電子数（TEC）を観測するため、小型衛星搭載用の電子密度・温度プローブ（EDTP）センサ、掩蔽 GPS (GPS-RO)、ビーコン信号送信装置を開発している。本研究の目的は、高度 60〜700 km の電離層におけるスラント方向及び垂直方向の電子密度の全球情報を取得するため、これら 3 つの円偏波アンテナシステムを開発することにある。円偏波信号の生成と軸比バンド幅（ARBW）を向上させるために、非対称の四角型切かけ付及び四角型寄生付の 2 種類の手法を用いたアンテナを提案した。小型衛星搭載用に適した仕様として、ビーコン信号送信装置用のアンテナは中心周波数 2.2 GHz、バンド幅 40 MHz、データ通信用アンテナは中心周波数 2.5 GHz、バンド幅 100 MHz を目標として開発を行った。四角型切かけ付の試作アンテナの ARBW の測定結果は 14.9%であり、これに対してシミュレーション結果の ARBW は 18.3%であった。バンド幅と利得をさらに向上するために試作した寄生付アンテナでは、周波数帯 2.16-2.95 GHz における 3-

dB の ARBW が 35.8%で、周波数帯 1.77-2.81 GHz の S パラメータの

バンド幅が 47.3%で、最大利得 5 dBic が週数数 2.2 GHz となった。

これらの数値は利得 4 dBic、ARBW と S パラメータの最低周波数帯

域 15.7%以上を満足したので、本研究の成果は広帯域、双方向パタ

ーン、コンパクトな構造が必要される小型衛星搭載広帯域円偏波ア

ンテナの実現になり、今後の電離層の研究への貢献が期待できる。

Acknowledgment

Contents

List of Tables

List of Figures

CHAPTER 1

1. INTRODUCTION

1.1 Research Motivations

In Global Positioning System (GPS) and Navigation Systems, the electron density in the ionosphere produces signal delays that cause range errors. In High Frequency (HF) from 3 to 30 MHz, radio signals can propagate to a very far receiver by skywave process, reflected by the ionosphere. Now, many researchers investigate the relationship between total electron content (TEC) and the electron density variation to global land deformation and earthquake events.

The range error in the ionosphere can be corrected in dual-frequency methods by a coherent phase combination in frequency L1 and L2. This error also can be corrected in the single-frequency method, with additional information that is corresponding to the total electron content and electron density of the ionosphere. So, TEC parameters play an essential role in the study of ionospheric dynamics and for forecasting, besides of correction for range error in a positioning system, and remote sensing applications.

The ionosphere is not a stable layer that supports the use of single-frequency throughout the months, weeks or even over in a day. The ionosphere alters with the seasons, the solar cycle, geographic and during any given day. The Sun goes experience a periodic rise and fall which affects ionosphere activity. At solar minimum, the ionosphere reflected only the lower frequencies, but

at solar maximum, the ionosphere will reflect and propagate the higher frequency of the HF band.

The total number of electrons between two points along a radio wave path is defined as TEC. 1 TEC unit (TECU) is 10^{16} electrons/m². Ionospheric TEC is predicted by measuring the carrier phase delays of received radio signals transmitted from satellites located above the ionosphere.

Josaphat Microwave Remote Sensing Laboratory (JMRSL) study and research the microsatellite development which uses payloads: Electron Density Probe and Electron Temperature Probe (EDTP) sensors, the GNSS-RO [1] and radio beacon [2]. The missions of this research are to provide atmospheric and ionospheric data such as the neutral atmosphere temperature, total electron content (TEC), the ionospheric temperature, and electron density. The ionospheric data are important to investigate the behaviors of electrons in the ionosphere, and the relationship between the ionospheric electron density fluctuation to the land deformation. The EDTP will collect the temperature and the electron density globally on the height of satellite orbit. The GNSS-RO receiver measures the TEC along the propagation path of radio waves transmitted by the GNSS satellites, which passed and refracted by the ionosphere and atmosphere [3]. The radio beacon transmits unmodulated, phase-coherent waves from satellite to receiver on the ground [4, 5].

The previous research for TEC and scintillation measurement used beacon signal has measurement methods such as 1. from space to ground named as CERTO beacon, 2. from space to space named as CITRIS and 3. from the ground to space named as Doppler Orbitography and Radio positioning Integrated by Satellite (DORIS) [4, 6]. The transmitter radio on satellites uses three frequencies band at the 1066.75 MHz, 400.32 MHz, and 150.01 MHz. The radiated effective power is around 1- 4 watt in Right-Handed Circular Polarization (RHCP). The three frequencies are received simultaneously in

the beacon receiver on the ground. The total electron content (TEC) between the satellite in space and receiver on the ground can be provided using two frequency (L1 and L2) with differential phase technique. The three frequencies were selected to enhance the scintillation area, to reduce noise effect, and TEC ambiguities. The CP antenna is tight to polarization mismatch, the effect of multi-path, and effect of the faraday, especially for satellites that relatively small size has no stabilization and attitude controller. The antenna was designed to give good radiation of the ground by using the crossed-yagi antenna. The crossed-yagi antenna uses phase shifter to generate CP wave.

The idea to use single-frequency GPS and Beacon measurements for ionospheric delay estimation and electron density are not new with a method of range code and carrier phase measurement, but until now, the literature on this research is relatively limited, mainly because of the code noise problem. TEC and electron density measurement presented in [7] by using single-frequency show result that TEC difference by single and dual frequencies commonly not exceeded 1.5 - 3 TECu. This method will reduce half of the transmitter power suitable for nanosatellite or picosatellite.

Now, an advanced electronic system makes it possible for the fabrication of nanosatellites and picosatellites that capable of performing simple and complex missions in space [8, 9]. However, a small satellite, especially for nanosatellite and picosatellite have limitations in size and power supply. Antenna for beacon [4] used the crossed-dipole Yagi is not suitable for a nanosatellite.

Microstrip antenna has relatively light, compact size and easy in fabrication, making this antenna type is suitable for a satellite system.

The objective of this research is to offer a novel circular-slotted antenna (CSA) having a wide CP operation, higher gain, small size, and relatively inexpensive in center frequency 2.2 GHz as requirements of the beacon sensor and communication onboard a small satellite or a nanosatellite. The

conventional CSA commonly offers small bandwidth [10, 11]. Generating CP wave, some methods proposed to a circularly-ring slot, for example, truncating two unsymmetrical rectangular slots on diagonal, inserting a parasitic patch, and shifting the feed line. The novel method proposed in this research is improving the axial ratio bandwidth by added a rectangular parasitic. This structure produces higher antenna gain and generates a bidirectional radiation pattern.

1.2 Research Contributions

The research contributions are summarized as follows:

- We have developed and fabricated a novel method to generate a circularly polarized (CP) wave in L band with center frequency in 2.2 GHz by making use of a pair of unsymmetrical rectangular truncation on the centered-circular slot.

- We have developed and fabricated a novel method to enhance the CP bandwidth of a CSA antenna for beacon frequency in 2.2 GHz with a bandwidth of 40 MHz and data communication 2.5 GHz with a bandwidth of 100 MHz by making use of a pair of the unsymmetrical rectangular truncation incorporated with parasitic path and shifted feedline.

- We have fabricated the antennas and measured its performance. The comparison of the simulated results and measured results show a good agreement.

1.3 Thesis Outlines

This thesis is compiled in five chapters, as expressed below :

- Chapter 1 provides the introduction, motivation, objective, contribution of this research, and outline of the thesis.

- Chapter 2 provides the background, theory, and context related to the materials discussed in the subsequent chapters. This chapter covers a description of the ionosphere, total electron content (TEC), techniques for TEC measurement by dual frequencies, single frequency, and the printed-slotted antenna.

- Chapter 3 provides the methods to generate circularly polarized waves and to enhance axial ratio for satellite and radio beacon. Improvement of the gain and the axial ratio of a wideband antenna is presented.

- Chapter 4 provides the experiment process and measurement results of the antenna type 1 and antenna type 2.

- Chapter 5 gives the research conclusion, contribution, and next works.

CHAPTER 2

2. BACKGROUND AND RELATED RESEARCH

2.1 IONOSPHERE

The atmosphere is stratified from ground to space with many layers due to the gravity of the earth. The known criterion is temperature. This defines the troposphere, stratosphere, mesosphere, and thermosphere, where the temperature decreases or increases alternately with height, as shown in figure 2.1 [12]. The transition region between the two layers is called a pause. The tropopause, in this case, separates the troposphere layer and stratosphere layer. Another criterion is based on the composition in the atmospheric. In the atmosphere, lower than 100 kilometers, the gases are mixed well and homogeneous. Turbulence mixes the air well-named turbosphere. At higher heights, diffusion is stronger than turbulence named the diffusosphere. Another criterion is also based on the atmosphere's physical behaviors such as electrons, ions, and the electric field [13].
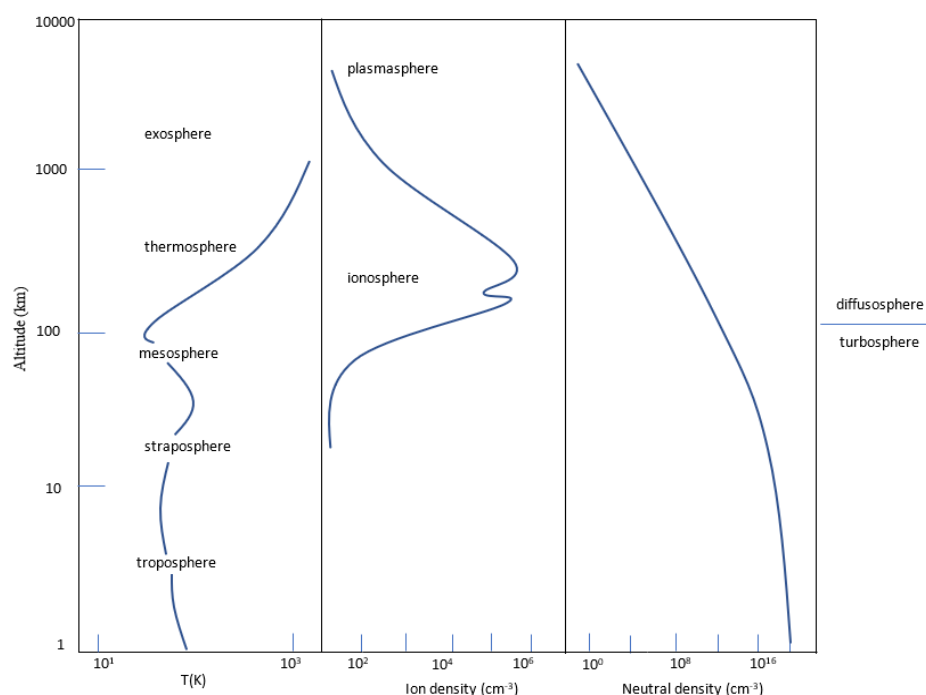
Figure 2. 1 The earth's atmosphere layer: the thermal structure in kelvin, the density of ion in cm^{-3}, density of neutral in cm^{-3}.

The ionosphere is atmosphere parts where the electrons and the ions affect the propagation of radio waves. These charged particles make the index of refraction for radio waves differ from unity. Electrons and ionized positive ions are created from the atmospheric gases by photoionization by extreme ultraviolet radiation. The sun is mainly the source of ionizing radiation. Additional minor sources are by energetic particles, solar wind, cosmic rays. The excess energy of the ionizing photons in the thermosphere rises the temperature, as the kinetic energy of the free electrons. The ionosphere is roughly 80 to 1000 kilometers altitude. At the height of around 450 km, the electron density reaches its maximum.

To identify the ionosphere layers, it labeled by the letters of D, E, and F. The D layer is the lowest until 80 km. This layer appears during the day affected

by the radiation of the sun. Recombination of ions and electrons is relatively quickly, caused by the density of the air that is still high in this layer. The next layer is labeled the E layer, above the D layer. This layer appears at a height from 100 km to 125 km. Ionization levels drops immediately caused by the electrons and ions recombine instantly after sunset. The E layer virtually disappears at night, overthought a small number of residual ionizations remains.

For long-distance and more stable communication, the F layer is very important. During the day, the F layer is divided into two sub-layers, like F1 and F2. At night, the two layers are combined into a single F layer. The F-layer height change depending on the time of day and the season.

The F1 layer is at around 300 km, and the F2 layer is at around 400 km or more, in the summer season. In the winter, it is about 300 km for the F1 layer and is about 200 km for the F2 layer. In the night, the F layer is generally around 250 to 300 km. In this layer, the rate of recombination is very slow, was caused the layer is higher, and air density is much lower. The ionization process remains until night, so it affects the radio waves.

The ionosphere has essential things on the earth as protection of life from the dangerous ionizing radiation from the sun and the universe. The photoionization process absorbed the radiation. The ionosphere affects the quality of communication, depending on the radio frequency we want to use. The limiting frequency in radio propagation by using the ionosphere is the frequency below that a wave component is reflected by, and the frequency above that it penetrates through an ionosphere. The critical frequency varies with atmospheric conditions and time of day as the result of electron limitation.

Ionosphere`s influence on radio propagation is such as reflection, scattering, absorption, refraction, as shown in figure 2.2.

Earth-satellite communications are influenced by the ionosphere [14]. Scintillation causes noise and unstable signal in communication links [15]. Refraction reduces the accuracy of the satellite-based navigation systems. The ionosphere reflects radio waves at frequencies below the plasma frequency [16]. These low frequencies are emitted by solar or other planets that are very important in astronomy. However, while we want radio communication between two points not passing the ionosphere, the ionosphere is very useful. The reflective properties of the ionosphere at a frequency below 30 MHz [16] make reliable communication between the transmitters and the receivers at a very far distance.
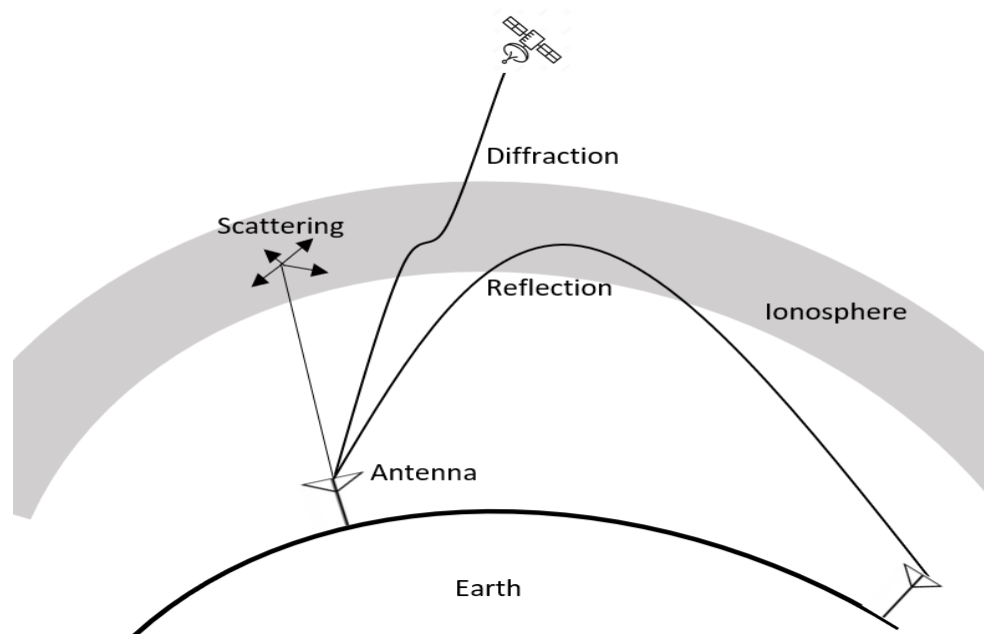
Figure 2. 2 Schematic of the ionosphere's effect on radio propagation
(left to right: scattering, diffraction, reflection).

The ionosphere is the earth's layer from about 80 until 1,000 km from the earth's surface which, consists of a high density of ions and electrons that capable of reflecting the radio waves. The essential parameters in the

ionosphere are the electron density Ne. Electron density varies with place and time. Because the ionosphere is stratified, the variation of electron density is higher in the vertical than the horizontal direction. The electron density of the ionosphere as a height function is called the ionosphere's vertical profile. Ionospheric TEC is determined by measuring the carrier phase delays of received signals that emitted from satellites located on middle orbit and low orbit, often using Global Positioning System satellites and beacon [17, 5]. The TEC is strongly correlated to solar activity.
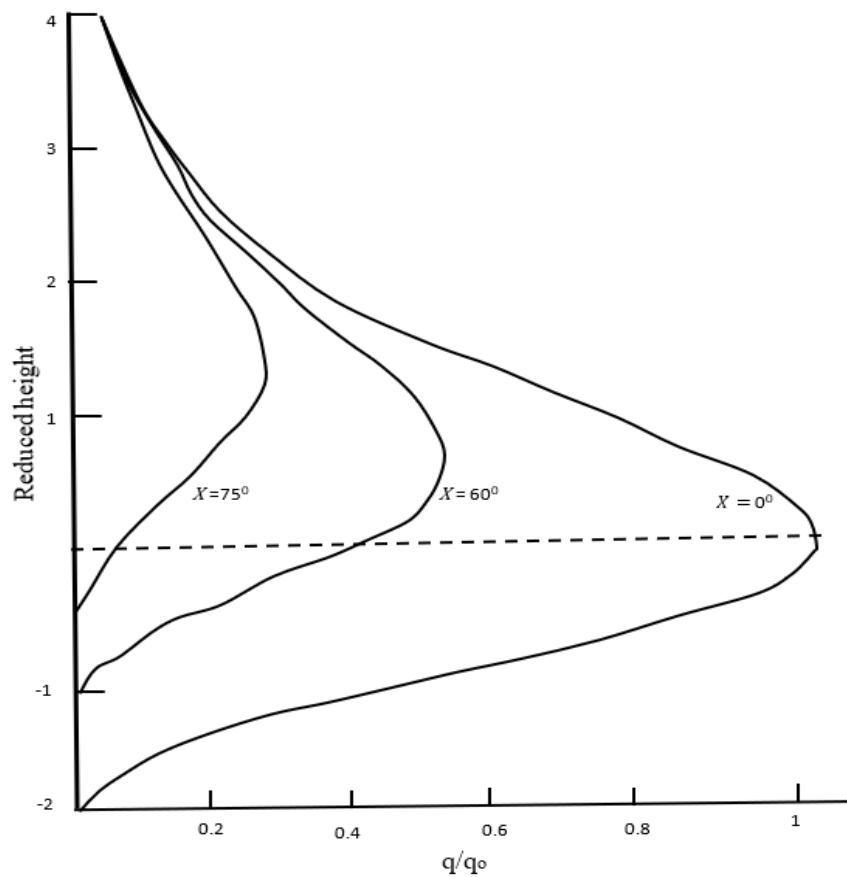
Figure 2. 3. Profile from Chapman model of ionization rate. [18]

The density of electron in the ionosphere differs with geographic latitude, longitude, season, the cycle of solar, and times of the day. Line integration of the vertical profile from the transmitter in space to receiver in-ground and vice versa gives the electron column density that is called TEC. Total electron content (TEC) is specified as the number of electrons on a line between two receivers in TEC$_U$, where 1 TEC unit (TECU) is 10^{16} electrons in squared meters. The TEC is an important parameter to determine the scintillation and phase delay of a radio wave passed a medium. Many researchers investigate the relationship between the electron density variation to global land deformation and earthquake events [19, 20].

There is a difference between vertical TEC and slant TEC. Slant TEC is the electron density in a column while the angle of the line of sight not 90 degrees between transmitter and receiver, and vertical TEC equals slant TEC while the line of sight is 90 degrees. Comparison of slant TEC while the angle of the line of sight varies from 0 degrees until 75 degrees (Figure 2.3).

2.2 OBSERVATION TECHNIQUES

Mainly, there are two methods to measure electron density of ionosphere: by in situ measurements or by remote sensing measurement. Now, many techniques for ionosphere monitoring, such as ground-based and space-based. In-situ measurements require sensors being placed in the ionosphere. These can be carried by installing the sensor on satellites to sense the ionosphere directly or by rockets launched into the lower ionosphere. Rockets have limitation in place and in time beside of these devices are very costly.

Remote sensing techniques enable the measurement of ionospheric electron density by radio wave transmission. Variation of radio wave parameters such

as the amplitude, the phase delay, the polarization, or the angle of arrival is used to calculate the density of electron in the ionosphere. Variations of the index of refraction of the ionosphere correlate to electron density, frequency. Many instruments for electron density measurement are such as ionosonde [21], incoherent scatter radar [22], global positioning system (GPS) [23,25] and radio beacon [24, 21]. The ionosonde is active radar that transmitted the radio wave from ground to ionosphere in sweep frequency from 1 MHz until around 20 MHz. The time difference between transmitted time and received time is related to the ionosphere height. An ionosonde is a radar ground-based, a powerful instrument for ionospheric research such as for TEC and density of electron, but operational of this instrument is relatively expensive, and it just measures the bottom side of the ionosphere layer. Figure 2.4 shows the method of ionosonde measurement.
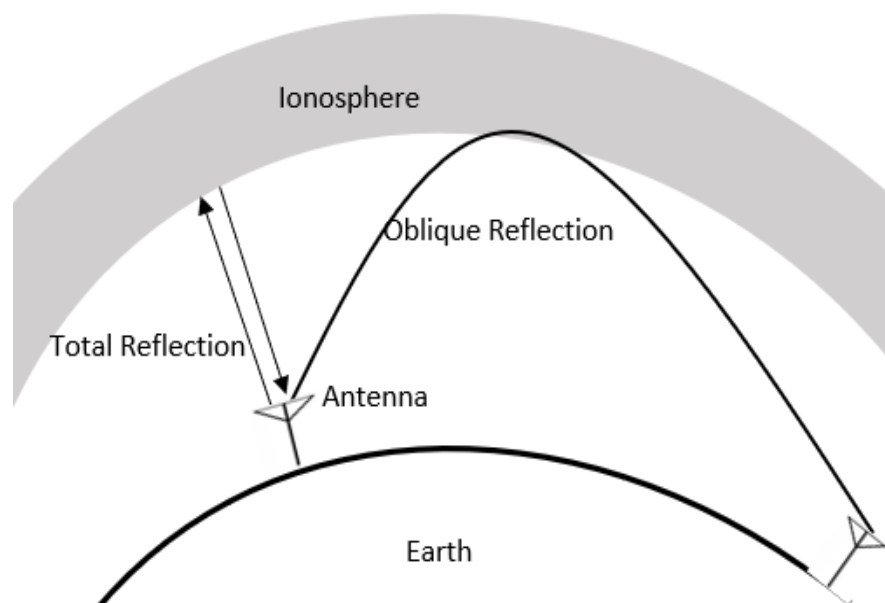
Figure 2. 4. Ionosonde (a) Total reflection (b) Oblique reflection

GPS satellites emit radio waves on frequencies of L1 in 1.57 GHz and L2 in 1.22 GHz. The velocity of a radio wave at the GHz band depends on the frequency and electron density of the ionosphere. This advantage enables us to extract the TEC in the line of sight from a satellite in space to the receiver on the ground. GPS is a space-based technique that orbited at an altitude of 20,200 km from the ground, as shown in figure 2.5, but in this measurement, the signal is strongly influenced by the plasmasphere layer.
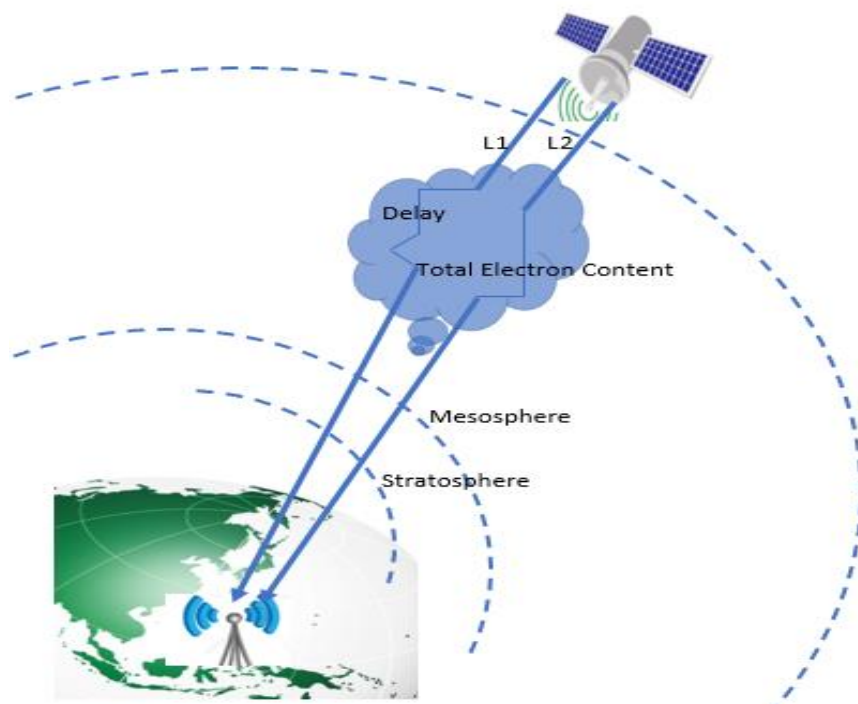
Figure 2.5. GPS and Beacon method for electron density measurement

For the dual-frequencies observation using GPS (L_1 and L_2), TEC in the slant direction is calculated from a combination of the pseudo-range (P) and phase observations (ϕ) as equation [2.1-2.3] below,

$$\text{TEC} = \frac{1}{40.3} \left(\frac{f_1^2 \, f_2^2}{f_1^2 - f_2^2} \right) (P_2 - P_1) \qquad [2.1]$$

$$\text{TEC} = \frac{1}{40.3} \left(\frac{f_1^2 \, f_2^2}{f_1^2 - f_2^2} \right) (\phi_2 - \phi_1) \qquad [2.2]$$

$$\text{TEC} = 9.52 \, (P_2 - P_1) \qquad [2.3]$$

where,

P_1 and P_2 are pseudo ranges, ϕ_1 and ϕ_2 are phases of carriers L_1 and L_2,

f_1 and f_2 are carrier frequencies of L_1 and L_2.

2.3 BEACON METHOD

Beacon is an electronic instrument transmitted radio wave which allows direction-finding equipment to find relative direction. This radio wave, which picked up by radio direction finding or systems for the angle of arrival on cars, buses, aircraft, and vehicles, will determine the direction to the beacon source. This radio beacon on satellite in low earth orbit transmit a signal to the ground receiver passed the lower ionosphere. The phase difference between these two signals determines TEC on the ionosphere.

Multi-antenna operation is required in order to have access to rising good links and communication from the transmitter on the space to receivers on the ground, as shown in figure 2.6.
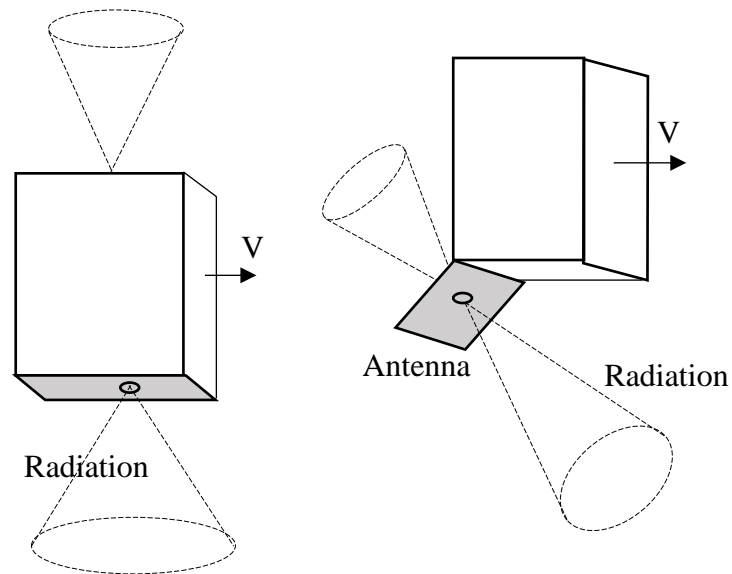
Figure 2. 6. Type of direction of antenna patterns

Meanwhile, satellite beacon at low earth orbit satellites (LEO) at an altitude of 750-1000 km provide ionospheric measurement results slightly affected by the plasmasphere layer. Receiver systems on the ground of the beacon signal measure the difference of phase of two signals in the frequency of 150 MHz and frequency of 400 MHz transmitted from low earth orbit to obtain the TEC value. The measurement technique is depicted in figure 2.5 and figure 2.7 below.
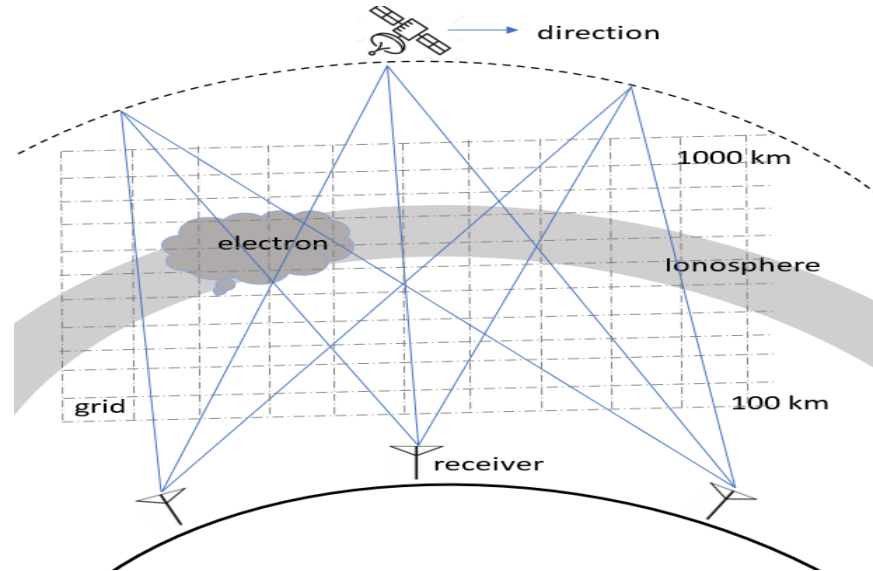
Figure 2. 7 Radio wave path, satellite trajectory and grid from 100-1000 km

The mathematic equation for TEC calculation based on the equation [2.4-2.6] below,

$$u = A \cos\left\{2\pi f\left(\frac{x}{c_p} - t\right)\right\} = A \cos\left\{2\pi f\left(\frac{nx}{c} - t\right)\right\} \qquad [2.4]$$

$$n = \frac{c}{c_p} = 1 - \{A/(2f^2)\}N \qquad [2.5]$$

$$\Psi = \frac{2\pi f L}{c} - \frac{\pi A}{cf}\int N\,dx + \eta \qquad [2.6\text{-a}]$$

$$TEC = \int N \, dx \qquad\qquad \text{[2.6-b]}$$

where,

u is a sinusoidal signal; A is the amplitude of signal; f is signal frequency; x is the distance from the satellite to the receiver; c is light speed, n is the index of refractive, N is electron density.

2.4 BEACON SENSOR ONBOARD SMALL SATELLITE

The ionosphere layer, which is the boundary in the atmosphere of the earth from 80 to 1000 km, has electrons and photons. Many instruments like satellites, rockets have already launched to study that region. The small satellite and microsatellite for ionosphere monitoring discussed in papers [26, 27]. Large size satellites have limitation to get more data in spatial beside of relatively expensive in manufacturing and launching to its orbit. A constellation of small satellites or nanosatellites provides more data in space sampling and time sampling. Although small satellite or nanosatellite has limitation in size and power, some nanosatellite concept is proposed for scientific mission [28, 29].

GAIA I is a microsatellite developed by Chiba University, in Josaphat Microwave Remote Sensing Laboratory (JMRSL), and National Institute of Aeronautics Space (LAPAN), is intended for getting the distribution of electron density in low altitude of 60 until 600 km in vertical of earth`s layer. For covering wider area of the ionosphere region are needed the complementary satellites which present more ionospheric data in time sampling and space sampling like beacon sensor.

The first step in the design process of an antenna for a satellite is to determine the specifications of the antenna as the proposed application. The specifications of the antenna have to be derived at the earlier stage from a mission requirement, the design and manufacturing of an antenna. The antenna specification is imposed by communications requirements, platform requirements, and mission aspects requirements.

The specification based on communication requirements is such as center frequency, dissipation factor, minimum antenna gain, bandwidth, polarization, and radiation pattern. The requirement for platform limitation is such as antenna size, weight, and compactness. The specification for mission requirements is such as antenna beamwidth, space-based material. The antenna in space must be strong enough for space environment such as for radiation of solar, magnetic field, for ionospheric plasma, for thermal condition and for launch condition.

Typical materials for antennas are metal alloys, polymer, ceramic, coating, and polymer composites. The metal alloy has a specification for thermal treatments, surface finish and corrosion protection. Polymers are such as thermoset resins, epoxy and thermoplastics. Polymer composites are based on carbon, glass, aramid, quartz fibers. The proposed antenna uses NPC-H220A with specification low dielectric loss for micro and millimeter-wave band, the dielectric constant of 2.17, dissipation factor of 0.0005 and flexing strength 50 N/mm^2.

The very important thing is the cost of the antenna. The total cost of research is as minimum as possible with maximum performance.

The diagram block of beacon transmitter is depicted in figure 2.8, that consists of a local oscillator (LO), frequency multiplier from 100 MHz to 2.2 GHz and 2.5 GHz, bandpass filter in 2.2 GHz and 2.5 GHz, power amplifier, directional coupler (DC) and a wideband antenna. Antenna for Tx beacon and for data telemetry [30] having bi-directional radiation patterns to overcome the

unstable direction to beacon receiver on the ground while the satellite spinning around. The solar panel is installed on 4 sides of the satellite for the supply of electricity, as shown in figure 2.9.
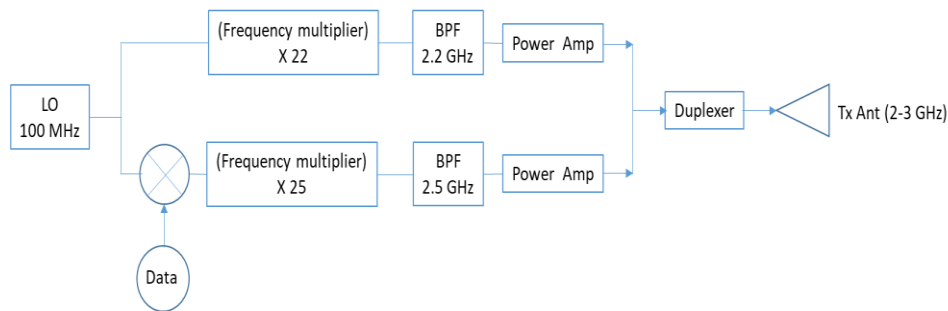
Figure 2. 8. Block diagram of the beacon transmitter and communication system
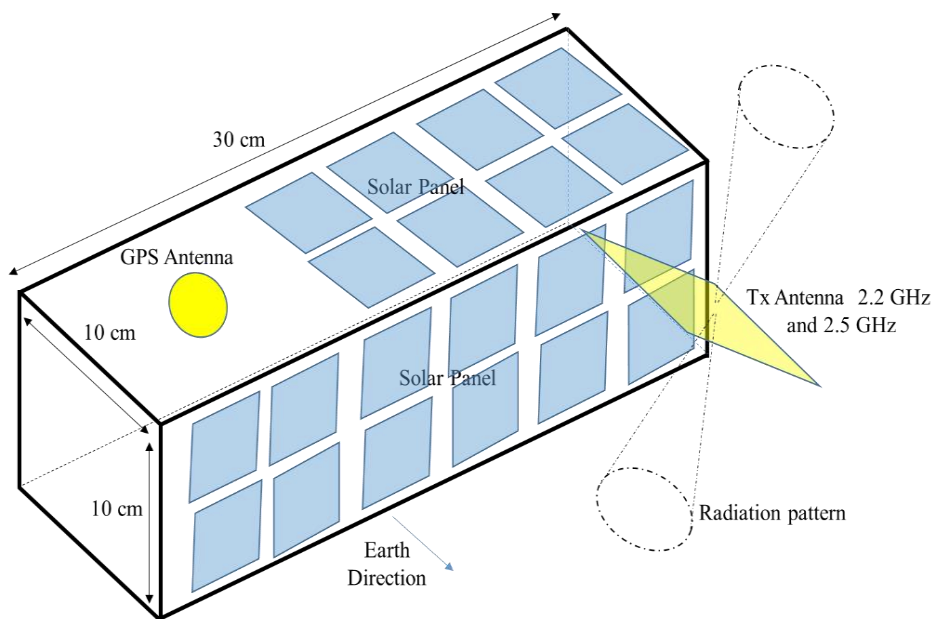
Figure 2. 9. Illustration of antenna position, tilted 45 degrees, for beacon transmitter in 2.2 GHz and data transmitter in 2.5 GHz

The intensity of the beacon signals on the ground receiver is calculated by assuming the emitted power of 1 watt from LEO orbit, the propagation distance of 3000 km, and bi-directional antennas at both points. Received power and voltage in a 50-ohm antenna induced at the ground antenna are around 4.9×10^{-15} watt and 4.9×10^{-7} volts in the frequency of 2.2 GHz. Illustration with a signal with a single frequency from space to the ground is shown in figure 2.10.
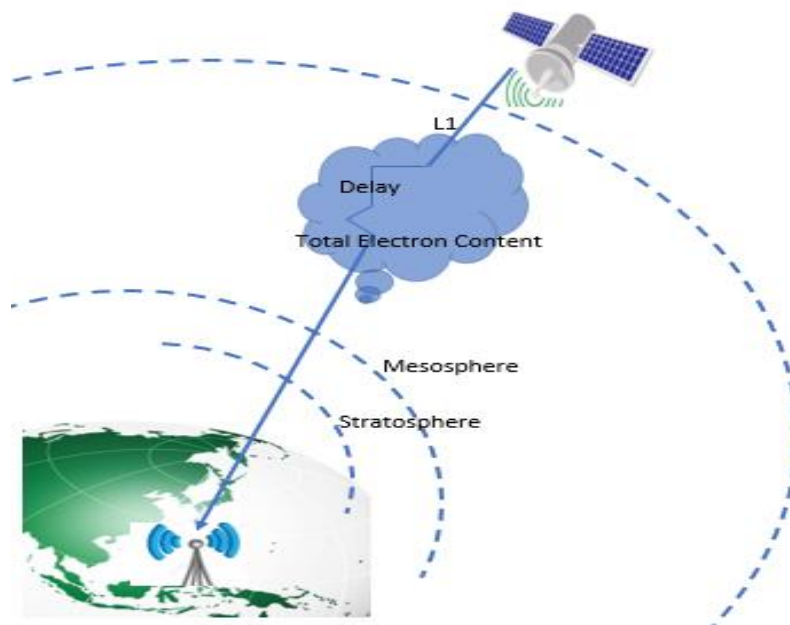
Figure 2. 10. Illustration of the beacon signal with a single frequency

2.5 CP PRINTED SLOTTED ANTENNA

Parameters of an antenna are determined by its reflection coefficient, impedance, polarization, gain, bandwidth, radiation beamwidth, and pattern. The reflection coefficient defines the total power reflected from the antenna to transmitter due to impedance of both the antennas is unmatched. If the reflection coefficient is 0-dB, it meant all radiated power is reflected. This condition can damage the transmitter system. Commonly, the acceptable minimum value for the reflection coefficient is -10 dB. It means the input power is delivered to antenna and emitted to space at least 90%, and the reflected power is around 10 %.

Gain is another useful parameter expressing an antenna performance. It is a measure that describes antenna efficiency and its directional pattern. The gain of the antenna determines the portion of power transmitted to the main direction from the power source in antenna input. The antenna gain is compared to an isotropic antenna having the gain of 0-dB, as shown on equation [2.7].

$$Gain = \frac{radiation\ instensity}{total\ input\ power}\ 4\pi = \frac{U(\theta, \emptyset)}{P_{in}} \qquad [2.7]$$

In microstrip antenna, rectangular and circular are the most common shapes, and both of them radiate similar broad patterns. Antenna size can be reduced by adding vertical shorting plates, slot-loading, high permittivity dielectric material, metamaterial and multi-feed.
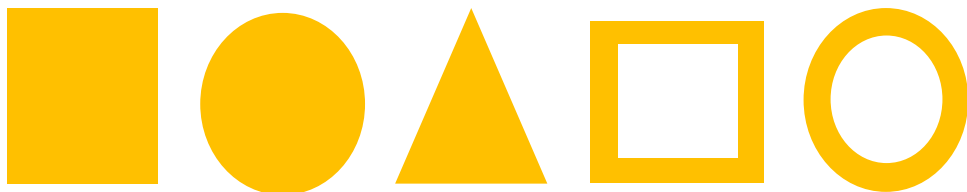
Figure 2. 11. Different geometries for compact microstrip design, in the rectangular, circular, triangular, square ring, and circular ring shapes.

The circular ring, square ring, and triangular patch have smaller areas compared to that of a circular patch and a square patch operating at the same resonant frequency, as shown in figure 2.11 and electrical current flow in figure 2.12.
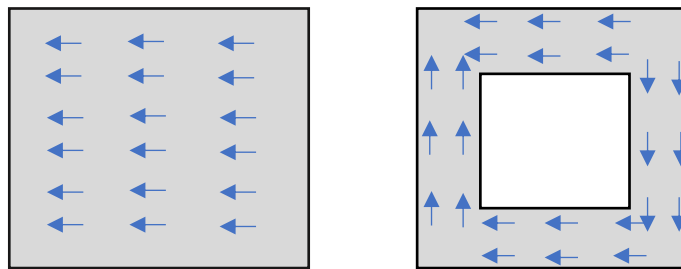
Figure 2. 12. The electrical current flow (indicated by the arrows) on a square patch and a square ring patch of the same size.

The basic equation for microstrip design will be approximately a half-wavelength long in the dielectric.

$$W = \frac{1}{2f_r \sqrt{\mu_0 \, \epsilon_0}} \sqrt{\frac{2}{\epsilon_r + 1}} \qquad [2.8]$$

$$L = \frac{1}{2f_r \sqrt{\epsilon_{reff}} \sqrt{\mu_0 \, \epsilon_0}} - 2\Delta L \qquad [2.9]$$

The resonant frequency f_r in hertz, the dielectric constant of the substrate ϵ_r, the height of the substrate h and extended on each end by a distance ΔL. The ΔL is a function of the effective dielectric constant ϵ_{reff} and the width-to-height ratio W/h.

The pattern of radiation is a graphical representation of the radiation properties in space coordinates [31] that described the distribution of power radiation and depicted in a three-dimensional coordinates system, as shown in Figure 2.13.
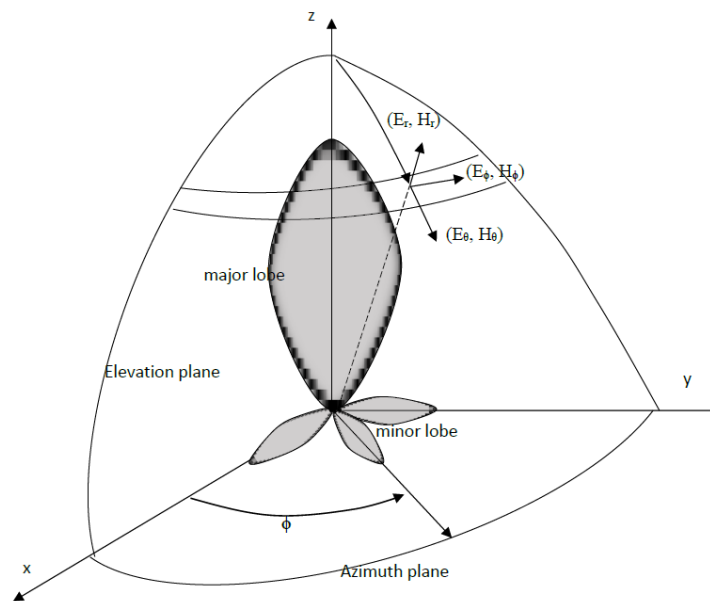
Figure 2. 13. The pattern of antenna radiation in a coordinate system

Mainly, there are three patterns of antenna radiation, such as isotropic (electric field intensity is similar in all direction), omnidirectional (similar power and electric field intensity in all azimuth angle but varying in angle of elevation) as depicted in Figure 2.14(a), and directional (the asymmetric pattern and most power or electric field intensity in the main beam) as depicted in Figure 2.14(b).

Solutions of Maxwell's equations as a plane wave is shown in equation 2.10

$$\vec{E} = \vec{E}_0 e^{i(\hat{k}\hat{x} - \omega t)}$$ [2.10]

$$\vec{B} = \vec{B}_0 e^{i(\hat{k}\hat{x} - \omega t)} \qquad [2.11]$$

$$\vec{B}_0 = \frac{1}{\omega} (\hat{k} \times \vec{E}_0) \qquad [2.12]$$

where,

$\vec{E}_0$ is called polarization vector for electric field and $\vec{B}_0$ is called the polarization vector for the magnetic field. The angular frequency ω and the wave vector $\hat{k}$ are related by,

$$|\hat{k}| = \frac{\omega}{c} \qquad [2.13]$$

Magnitudes of electric field and magnetic field are related by equation 2.14

$$|\vec{E}_0| = c\,|\vec{B}_0| \qquad [2.14]$$

In-plane wave, the polarization vector of the electric field $\vec{E}_0$, the magnetic field $\vec{B}_0$, and the direction $\vec{k}$ are all orthogonal.

The equation for the electric field which propagates in the z-axis is expressed as in equation 2.15 below,

$$\vec{E} = \vec{E}_0\, e^{i\omega(\frac{z}{c} - t)} \qquad [2.15]$$

where,

$\vec{E}_0 = (E_x, E_y, 0\,)$

E_x and E_y have amplitudes and phases. In the exponential form, we can write as equation below,

$$E_x = |E_x|\, e^{i\varphi_x} \qquad [2.16]$$

$$E_y = |E_y| \, e^{i\varphi_y} \qquad\qquad [2.17]$$

In polarization vector, we consider the relative size of E_x, E_y and the phase difference $\varphi = \varphi_x - \varphi_y$.

The antenna polarization is determined by its orientation of the electric field emitted by an antenna. If a half-wavelength is oriented in vertically above the Earth, it will radiate fields in the far-field dominated in $E_\theta(\theta, \varphi)$. In this case, the polarization is called vertical polarization. If a half-wavelength is horizontally oriented above the Earth, the radiated electric fields to be dominated in $E_\varphi(\theta, \varphi)$ the direction in the far-field.
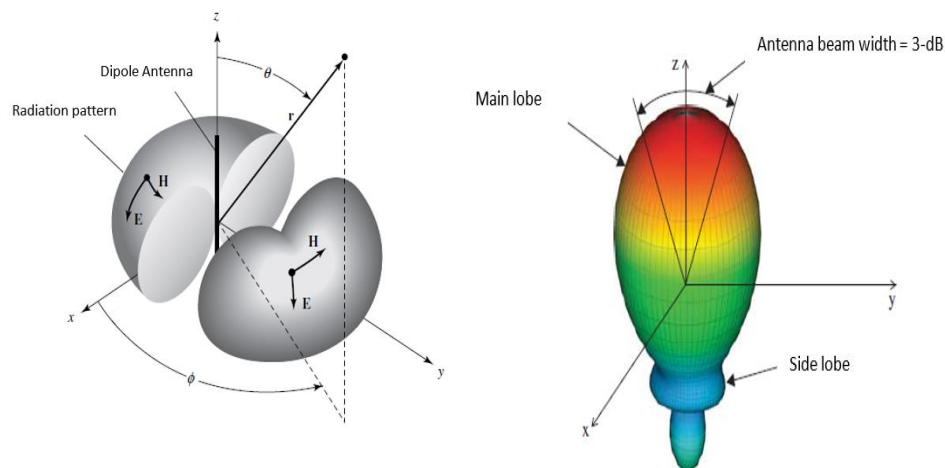

Figure 2. 14 (a). Omni-directional pattern (left), (b). Directional pattern (right)

The polarization of the antenna is then called horizontal polarization. Both horizontal and vertical polarizations are linear polarization as shown in figure 2.15.

The electrical field emitted by an antenna can be expressed as shown in equation [2.18] below,

$$\vec{E}(\theta,\varphi) = \vec{\theta}\, E_\theta(\theta,\varphi)e^{j\phi_1} + \vec{\varphi}\, E_\varphi(\theta,\varphi)e^{j\phi_2} \qquad [2.18]$$

Here, the magnitudes of the electric field components in the far-field of the antenna is denoted of $E_\theta(\theta,\varphi)$ and $E_\varphi(\theta,\varphi)$ respectively.
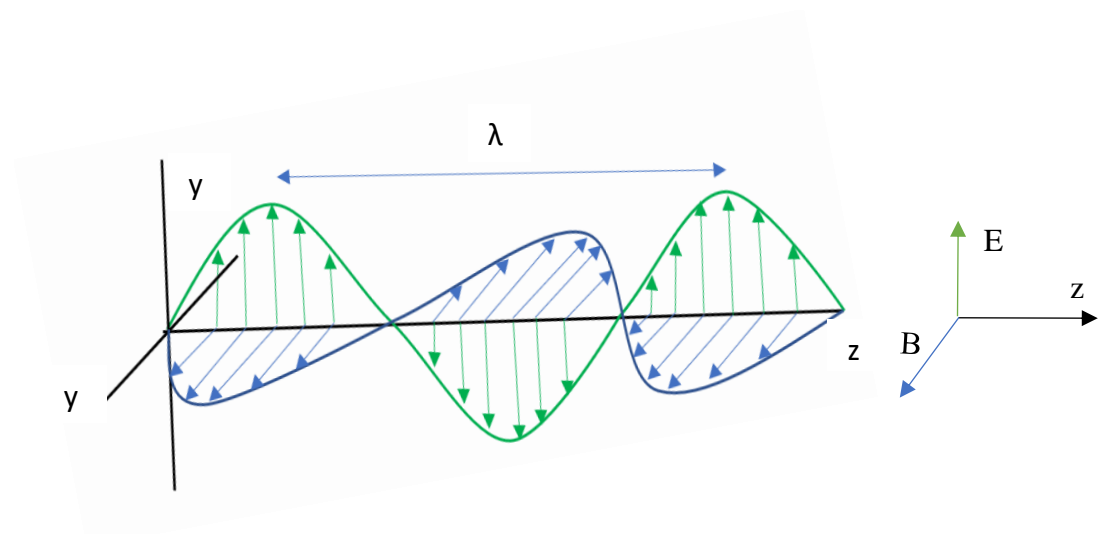
Figure 2. 15. Electric field and magnetic field in linear polarization

For a plane wave, if there is no phase difference between E_x and E_y in a cartesian coordinate system or $E_\theta(\theta,\varphi)$ and $E_\varphi(\theta,\varphi)$ in a polar coordinate system, the wave is linearly polarized, as shown in equation 2.19 below.

$$\vec{E_0} = (E_x, E_y, 0\ ) \qquad [2.19]$$

If $E_y = 0$ and $E_x \neq 0$, the wave as shown in equation 2.20 below,

$$\vec{E} = E_0\hat{x}e^{i(kz-\omega t)} \qquad [2.20]$$

To generate CP wave, it must generate the electric fields with two orthogonal components in the far-field area, as shown in Equation 2.5.

Circular polarization can be achieved only if the electric field has two orthogonal signals which have the same magnitudes and a 90^0 phase difference of the two components, as shown in equation [2.21, 2.22] below.

$$E_\theta(\theta, \varphi) = E_\varphi(\theta, \varphi) \qquad\qquad \text{[2.21]}$$

$$\phi_2 - \phi_1 = \pm \frac{\pi}{2} \qquad\qquad \text{[2.22]}$$

The antenna bandwidth has specified the interval of frequencies within which the performance of the antenna fulfilled to a determined-parameters. The electric field and magnetic field in circular polarization is shown in figure 2.16. The antenna parameters such as the impedance of input, pattern, beam width, polarization, gain, radiation efficiency in frequency interval with an acceptable value. The input impedance is commonly specified under 10 dB as an acceptable value for input impedance bandwidth. An antenna with circular polarization has specified standard as the axial ratio bandwidth while the value is under 3-dB.
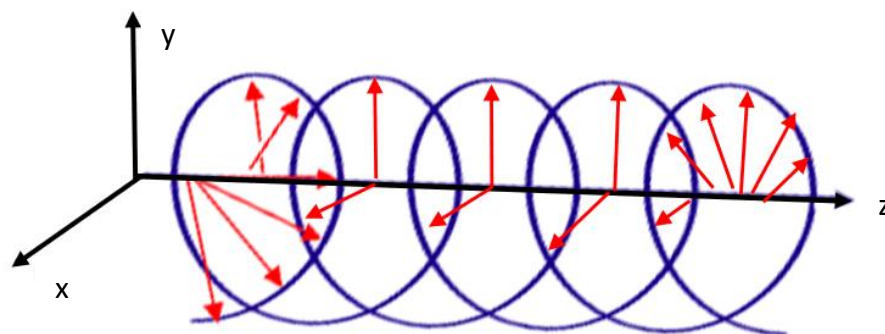

Figure 2. 16. Electric field and magnetic field in circular polarization

2.6 RELATED RESEARCH

Many antennas in linear and circular polarization have been proposed for small satellites and nanosatellites, such as for GPS transmitter and communication systems [32, 33, 34].

Some of them are a single narrowband or a wideband antenna, and the others use a dual-band frequency with narrowband. CP antennas proposed and designed for the satellite GPS, and Galileo is a helix antenna with a bifilar design [35], a slot antenna with an annular-ring shape [36], and spiral having six turns [37]. Some antennas with dual bands are proposed for the GNSS receiver: a stacked patch with a branched-line hybrid feeding line and proximity probes [37] and a microstrip antenna having dual-connected probes [38].

Meanwhile, antenna for data transmission also adopts a circular polarization wave. Communication antennas in S-band have been presented, such as spirals with conical shape [34], [39], helix antennas with the quadrifilar design [40], [34], antennas with a conical linear spiral [41] and with parasitic elements [42]. Thus, an investigation of the antenna`s characteristics with small size, and lightweight is necessary. Circularly Polarized (CP) antennas are very important for satellites because of their strength to multi-path effects, polarization mismatch, and Faraday`s rotation effect.

Faraday`s rotation is a magnetic and optical phenomenon, as an interaction between a magnetic field and light in a medium. The Faraday`s rotation causes a spin of the polarization plane, that is proportional to the part of the magnetic field in the direction of wave propagation. This phenomenon

happens in most optically transparent dielectric materials under the influence of the magnetic field.

Particularly for nanosatellite, the circularly-polarized antenna with the wide beam is very important, because the angles in elevation and in azimuth are uncertain position. The CP microstrip antennas have been broadly developed for the satellite antenna by considering its compact size and also relatively lightweight, which is a critical issue for small satellite nanosatellite.

A printed-slotted antenna has advantages compared to the above-discussed antennas for satellites and others for space-based applications. Based on the feeding line method, microstrip-slotted antenna, mainly has two methods: 1). a coplanar waveguide (CPW) feed, commonly generate a wider bandwidth and 2). a microstrip feed line commonly generates a higher antenna gain. The first method is classified into a wide slot and a ring-shaped slot.

Commonly, antennas with a ring-shaped slot generate narrower bandwidth compared to an antenna with a wider slot, but it provides a smaller size of the antenna. By enlarging the size of the slot, the 3-dB axial ratio bandwidth can be improved.

It is presented that a slotted antenna having an annular-ring shape fabricated on an RT 5880 laminate reaches the 3-dB axial ratio bandwidth until 65% in frequency of L band [36]. A slotted antenna with a squared-ring design printed on an FR4 laminate generates the 3-dB axial ratio bandwidth of 45% at a frequency of 3.32 GHz [43]. The wider 3-dB axial ratio of 68%, the maximum gain of 4.0 at 4 GHz, is produced by an antenna with CPW-feeding line, two diamond-shaped wide symmetric apertures [45]. An antenna with CPW-fed having squared-slot and three inverted-L-shape fragments achieves the 3 dB AR bandwidth of 80% [45].

The literature of antennas for beacon proposed for total electron content (TEC) measurement that using two frequencies is very limited, as discussed in [6, 44], but these antennas have the unappropriated size and unpractical for

a nanosatellite. In reference [47] proposes a dual-band circularly-polarized antenna in UHF-band and S-band with microstrip antenna, but this antenna produces a relatively narrow impedance and axial ratio bandwidth.

CP printed-slotted antennas have been proposed to widen the 3-dB axial ratio powered with a coplanar waveguide and a microstrip feeding line. A slot antenna fed by coplanar waveguide having a lightning-shaped feeding line and inverted-L strips [48] produces the 3-dB axial ratio of 48.8% and achieves peak gain around 3.4 dBic. A coplanar-fed stair-shaped slot antenna [49] produces the 3-dB axial ratio of 31.2%, and the gain achieved 3.7 dBi. Antenna, with a ring slot powered by microstrip-line, has a narrow bandwidth of more than 6 %, such as presented in [50]. Higher gain has been achieved by a wide-slotted antenna having air between microstrip-line-feeding and reflecting plate, as presented in reference [51]. The antenna produces the 3-dB ARBW of 12 % and obtains an antenna gain of 5.5 dBic. A circular-shaped-slotted antenna presented in reference [52] achieves the 3-dB axial ratio of 44 % in frequency 2.9-4.5 GHz and obtains a peak gain of 5 dBic.

The conventional circularly-slotted antenna generates linear polarization. Circular-ring-slotted antenna fed by strip line in [53] transforming linear to circular polarization produces the 3 dB axial ratio bandwidth of 9 %. Modifying the structure of patch, such as introduces an annular ring slot and a hybrid coupler [54], produces 75 MHz, but the antenna gain is lower than 2.5 dB. In [55], two linked-slotted rings enhance the axial ratio bandwidth of 2.65-3.7 GHz, but antenna gain until 2 dBic. Nevertheless, the methods proposed previously yield the 3-dB axial ratio narrower than the impedance bandwidth of the antenna. A new technique is necessary to broaden the 3 dB ARBW. Methods for this goal, by including a rectangular-shaped-slanted slot on a circular-shaped patch [56] and by a narrow slot horizontally on a triangular-shaped patch antenna [57]. However, these methods did not

succeed to enhance the impedance bandwidth, the 3-dB axial ratio bandwidth, and the antenna gain.

Table 2. 1 Performance comparison of circularly-polarized (CP) slot antennas

Reference	f_c (GHz)	3 dB (ARBW) (%)	(IBW) (%)	Peak Gain (dBic)	Dimension (mm)
[42]	3.625	68	107	4	60 x 60 x 1.6
[46]	2.745	48	51	4.2	60 x 60 x 0.8
[48]	1.59	6.3	14.7	3.6	54 x 54 x 1.6
[50]	2.375	12	39	5.5	120 x 120 x 33
Proposed	2.2	35.8	47.3	5	95 x 100 x 1.6

The CP wave was produced by adding two truncations, a simple feeding line having 50 ohms, and an additional parasitic patch. Truncations were realized by two asymmetrical slots with rectangularly-shaped to generate circular polarization wave. The feeding line is moved to the negative side, *x*-axis, to raise the gain. Added a stub on the head of the feeding line to tune the impedance. The 3-dB axial ratio improvement of the CSA, a rectangularly-shaped parasitic, is added into the circular-shaped slot, which generates the second resonance in higher frequency.

The dimensions and performance of the fabricated antenna are compared to other CP printed-slot antennas summarized in Table 2.1. The proposed antenna has a higher peak gain compared to those reported in reference [44, 48, 50], has a broader 3 dB ARBW compared to reference in [48, 50], and has a smaller size compared to reference in [51].

CHAPTER 3

3. WIDEBAND CP ANTENNA FOR SMALL SATELLITE AND COMMUNICATION

This thesis describes 2 simulated and fabricated antennas named antenna type 1 and antenna type 2. The design of antenna type 1 and antenna type 2 is almost similar, but antenna type 2 has a wider 3-dB axial ratio bandwidth by added a rectangular-shaped parasitic patch on the circular slot.

Antenna type 1 can be used for the beacon antenna in the frequency of 2.2 GHz and use another antenna for data communication. Nanosatellite has limitations in size and power supply. Antenna type 2 will overcome the problem of the size limitation with the modification design having a wider 3-dB axial ratio bandwidth.

Antenna type 2 proposed for beacon antenna in 2.2 GHz with bandwidth around 40 MHz and a communication system at 2.5 GHz with bandwidth around 100 MHz. The antenna is developed on the printed circuit board (PCB) material and substrate material which has a relative permittivity ε_r is 2.17, the thickness is 1.6 mm, the loss tangent is 0.0005. The copper on the top side and bottom side of the substrate has a thickness of 0.035 mm.

Both antennas, type 1 and type 2, are designed and fabricated based on CSA design. The novel techniques proposed here are changing the polarization of conventional CSA microstrip antenna from linear to circular and widening the 3-dB axial ratio bandwidth. The first technique introduces unsymmetrical rectangular truncation on CSA diagonal, then called type 1 of CSA antenna. The second one employs a combination of unsymmetrical rectangular truncation and a rectangular parasitic on the slot.

3.1 CIRCULARLY-SLOTTED ANTENNA (CSA)

The antenna of type 1 is printed on a single substrate, that consists of the grounding in the front side, and the feeding line on the bottom side of the substrate. The antenna is designed with a square patch, with length size (L) of 100mm and width (W) of 100mm. A slot with a circular form is developed in the center of the patch with a radius (R) of 26.5 mm. Grounded patch has two asymmetrical rectangular truncations with the width size of (W_s) of 16 mm, length size of (L_{s1}) of 48 mm and (L_{s2}) of 42 mm. The feeding line has a bottom width (W_{f1}) of 4.5 mm, up width (W_{f2}) of 10 mm, the bottom length (L_{f1}) of 40 mm, the up length (L_{f2}) of 8mm. The detailed geometry of the CSA is depicted in Figure 3.1.
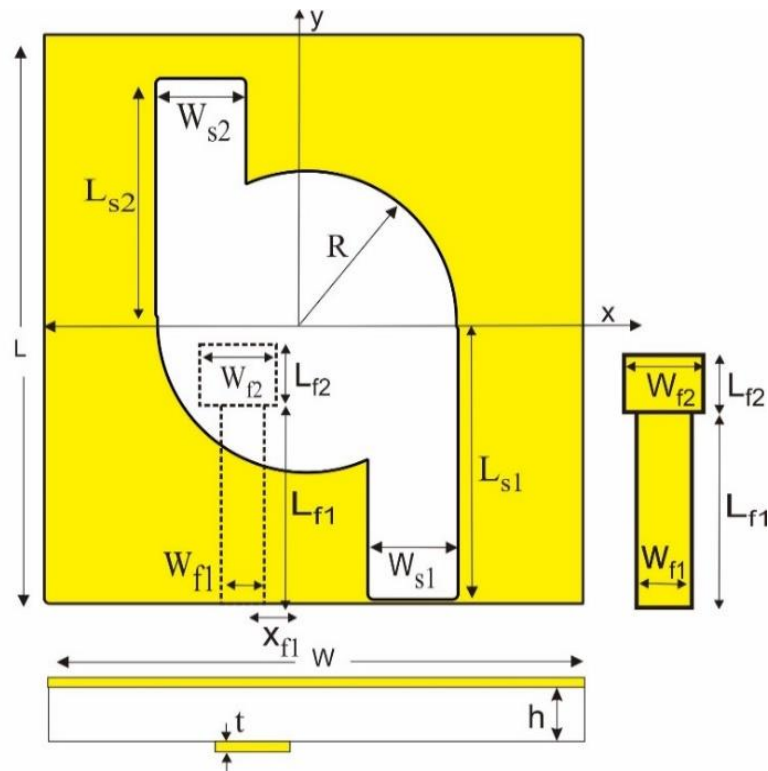
Figure 3. 1 Design of the antenna with a circularly-slotted, shifted, and deformed feeding line and truncation on the diagonal patch.

3.2 GENERATION STEPS FOR CIRCULAR POLARIZATION WAVE

The steps for the generation of circular polarization waves are in 3 steps. Step 1 is a conventional model having a square patch with a slot on patch center with radius (R), the width of the feeding line W_{f1} and W_{f2}, and the length of L_{f1} and L_{f2}. The conventional model has a circular slot, and the feeding line shifted on the x-axis of X_f as depicted in Figure 3.2.a. Step 2 consists of a shifted feedline of X_f and added two rectangular truncations with equal length of L_{s1} and L_{s2} on the patch diagonal, as depicted in Figure 3.2.b. For

tuning the impedance frequency center is by deforming the feeding line with modifying the upper feedline W_{f2} wider than bottom feedline W_{f1}. Step 3 is to modify the truncation with an asymmetrical length of L_{s1} and L_{s2}. The truncation L_{s1} is longer than L_{s2} as shown in Figure 3.1 as the final step of the type 1 antenna.
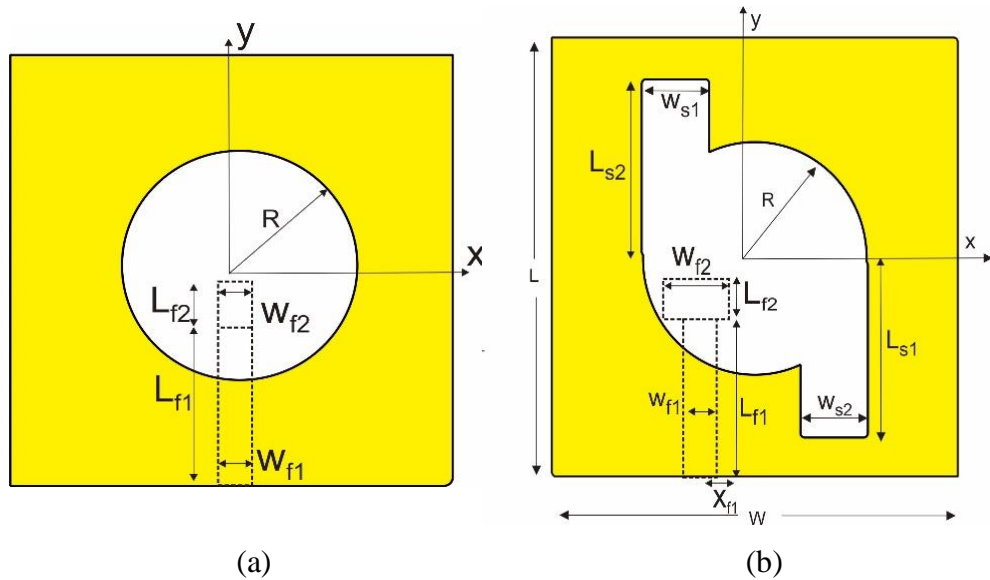

(a)   (b)

Figure 3. 2 Design of the antenna models. (a) step 1 as a conventional model. (b) step 2.

Figure 3.1, 3.2 depicts steps to generate circular polarization wave, started from step 1 as a conventional model, step 2, and step 3. Dimensions in detail the proposed antenna are shown in Table 3.1 Comparison of the simulated design of the model steps, model 1, and model 2 is showed in figure 3.3 and is summarized in Table 3.2.

Table 3. 1 Dimension of the Antenna in step 1, step 2 and step 3.

Steps	L (mm)	W (mm)	R (mm)	L_{s1} (mm)	L_{s2} (mm)	W_{f1} (mm)	W_{f2} (mm)	X_{f1} (mm)
Step 1	100	100	26.5	no slot	no slot	3.8	3.8	0
Step 2	100	100	26.5	42	42	3.8	3.8	-5
Step 3	100	100	26.5	48	42	4.5	10	-5

Table 3. 2 Result of simulation in step 1, step 2, and step 3.

| Steps	$f_c ibw$ (GHz)	IBW(GHz), %	$f_c$arbw (GHz)	3-dB ARBW (GHz), %	Gain (dBic)
Step 1	2.20	1.99-2.65, 30.22	none	none	2.5
Step 2	2.25	2.06-2.97, 40.57	2.23	1.97-2.5, 23.76	2.46
Step 3	2.1	1.76-3.17, 67.4	2.23	2.02-2.43, 18.3	4.2
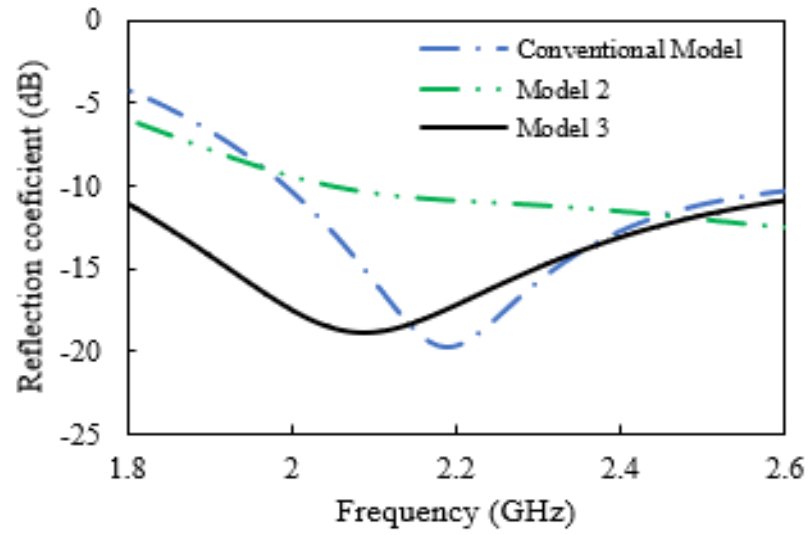
(a)
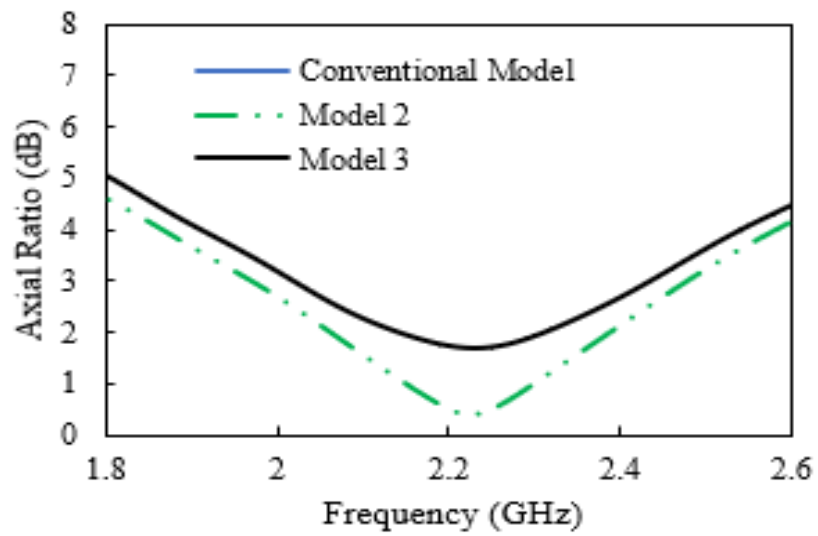
(b)
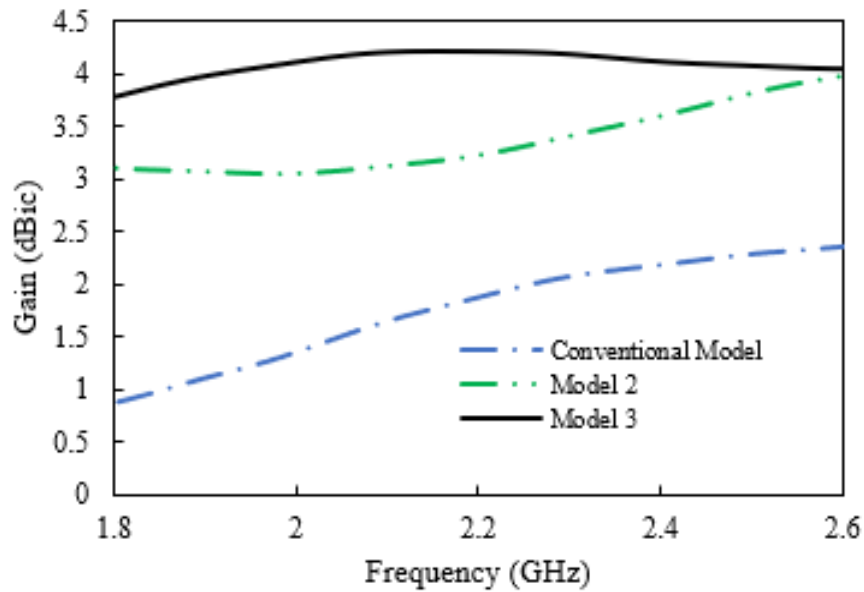
(c)

Figure 3. 3 Comparison Results (a) the reflection coefficient (S_{11})
(dB); (b) the axial ratio of antenna (dB); and (c) antenna gain (dBic).
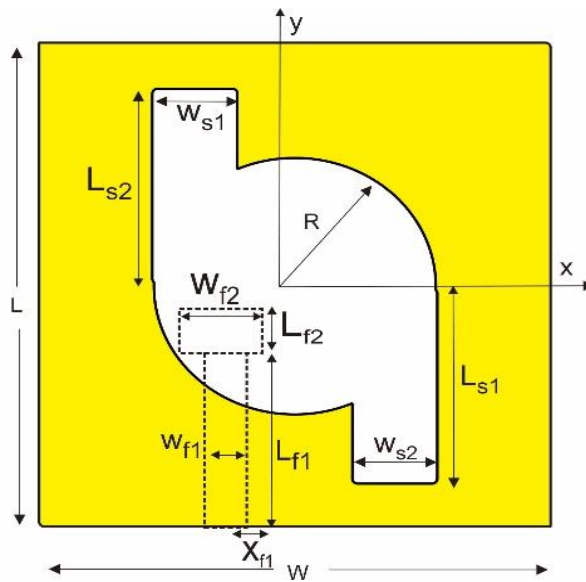
3.3 AR ENHANCEMENT WITH TRUNCATION AND A PARASITIC PATCH

The steps for designing the antenna consist of model conventional, model 1, as depicted in Figure 3.4.(a), (b). The conventional design of CSA, as illustrated in Figure 3.4 (a), generates the linear polarization radiation. The radius (R) of the slot determines the resonant frequency of the antenna. The antenna is simulated on a substrate with a relative permittivity (ε_r) of 2.17, thickness (*h*) of 1.6 mm, loss tangent of 0.0005, and slot radius (*R*) of 26.5 mm. The antenna of type 2 having a width (*W*) of 95 mm and the length *(L)* of 100 mm generates the resonant frequency of 2.17 GHz. The feedline as

depicted in figure 3.4. (a) has a length L_{f1} of 40 mm, L_{f2} of 8 mm, width W_{f1} of 4 mm, and W_{f2} of 4 mm. Figure 3.5 depicts the final design, named as antenna type 2. The dimensions of the CSA model are shown in Table 3.3.
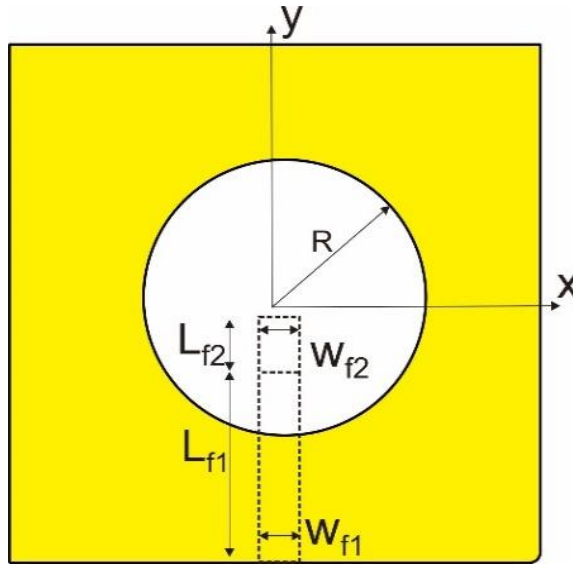
(a) Step 1 as conventional model

(b) Step 2 with rectangular truncation

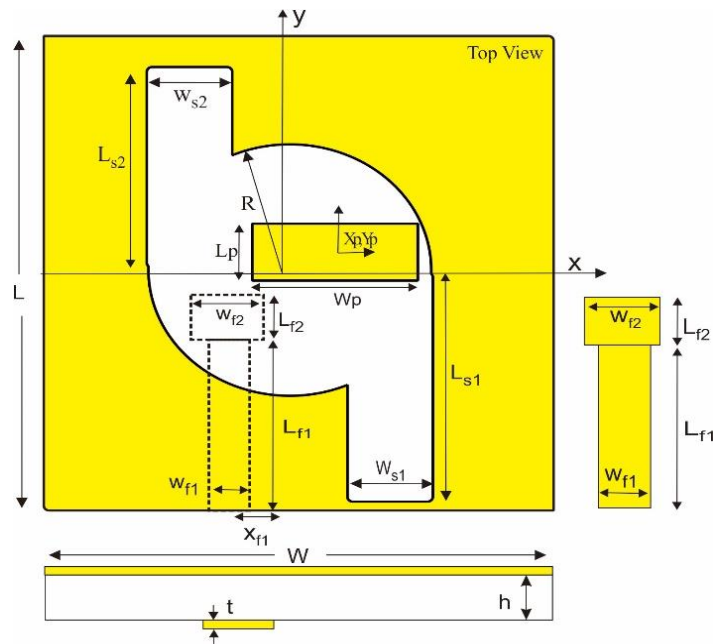Figure 3. 4 Geometry of CSA; (a) Step 1 as conventional model (b) Step 2

Figure 3. 5 The geometry of antenna type 2. The feed line and the edge profile are drawn on the right side and the bottom side, respectively.

Table 3. 3. Dimensions of CSA, from step 1, step 2, and step 3.

| Steps	R (mm)	L_{s1} (mm)	L_{s2} (mm)	W_{f1} (mm)	W_{f2} (mm)	X_{f1} (mm)	L_p mm)	W_p (mm)	X_p (mm)	Y_p (mm)
Step 1	26.5	-	-	4	4	0	-	-	-	-
Step 2	26.5	40.79	40.79	4	4	-9	-	-	-	-
Step 3	26.5	48	40	4	10	-9	12	31	8	5

3.3.1 A Pair Symmetrical Rectangular Truncation

Antenna with circular polarization wave is produced from the linear polarization antenna by modified the truncation [58, 30] and shifting the feeding line to the left and right side from the center. This step shifted the feeding line to the negative side of the x-axis and added two symmetrical rectangular-shaped slots. The feeding line is moved to the negative side X_{f1} of 9 mm. The rectangular-shaped truncation has a length L_{s1} of 40.79 mm from the origin, the width W_{s1} of 16 mm and L_{s2} of 40.79 mm from the origin, the width W_{s2} of 16 mm. This design generates the circularly-polarized wave and enhances the gain. The length of L_{s1} and L_{s2} influences the resonant frequency by reason of it changes the slot size. The longer of L_{s1} the higher the resonant frequency. This step is achieved a wider impedance bandwidth than the conventional model one. Effects of the truncation length to reflectance coefficient, axial ratio, and antenna gain, as shown in Figure 3.6. The truncation length varies from 0 mm, 30 mm and 40.79 mm. While the truncation length of 0 mm, the center frequency of the reflectance coefficient is shifted to the frequency of 2.37 GHz, and the bandwidth of impedance achieve until 1.11 GHz. The antenna obtains a gain of 1.92 dBic in 2.2 GHz and reaches a gain of 2.4 dBic on the frequency of 2.6 GHz. While the length of the slot extended to be 30 mm, the center of frequency is moved to 2.59 GHz, the frequency higher than before. This step model reaches the gain in 4.06 dBic.
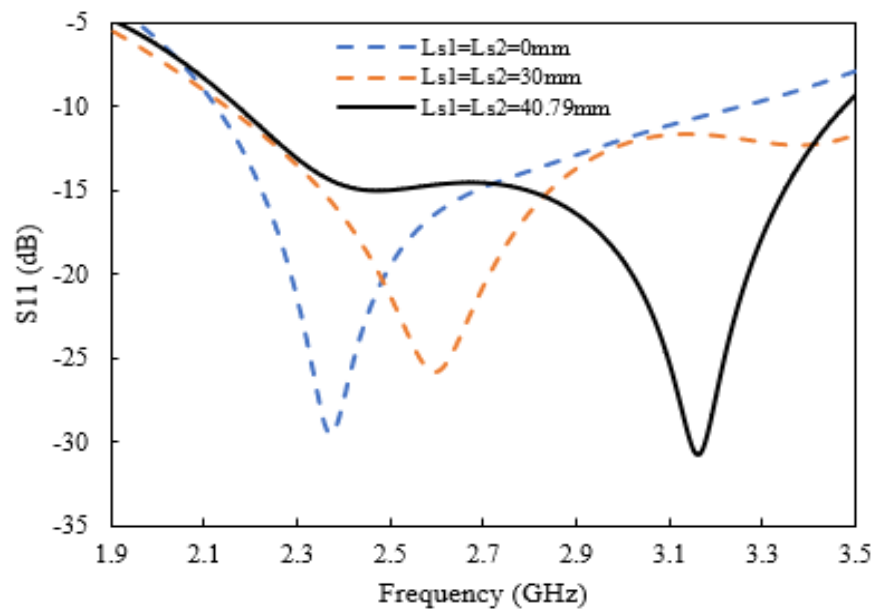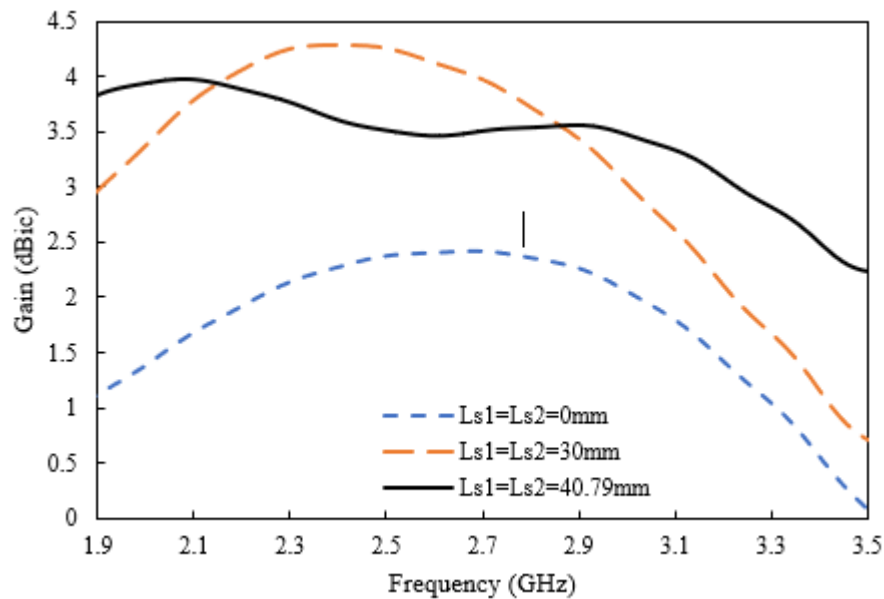
(a)
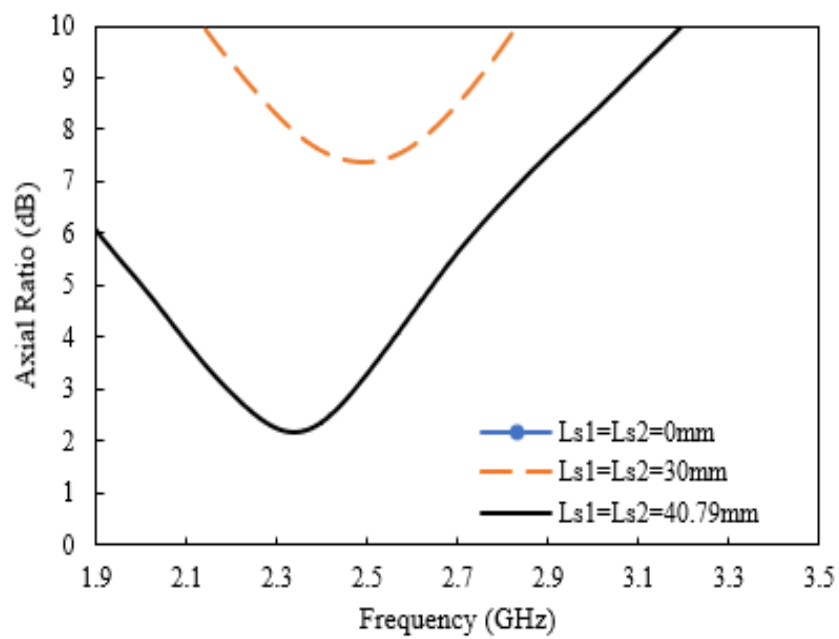
(b)

(c)

Figure 3. 6 (a) S_{11} (dB) (b) Axial ratio (dB) and (c) antenna gain (dBic),

while truncation length varies from 0 mm, 30 mm and 40.79 mm

But the weakness of this design, it fails to generate the axial ratio value smaller than 3-dB. While the rectangular truncation length to be 40.79 mm, it generates the 3-dB axial ratio at the center frequency of 2.34 GHz and generates the 3dB bandwidth of 270 MHz. While the length of truncation is extended more than 40.79 mm, the 3-dB axial ratio to be wider, but the resonance frequency of the reflectance coefficient is moved to the higher frequency.

3.3.2 Rectangular-shaped Parasitic Patch

Improvement of the CSA is needed to enhance the 3-dB axial ratio performance. Antenna in step 1 has the 3-dB axial ratio narrower than

impedance bandwidth. Many techniques were proposed to improve the 3-dB axial ratio, such as by parasitic patch [59, 60].
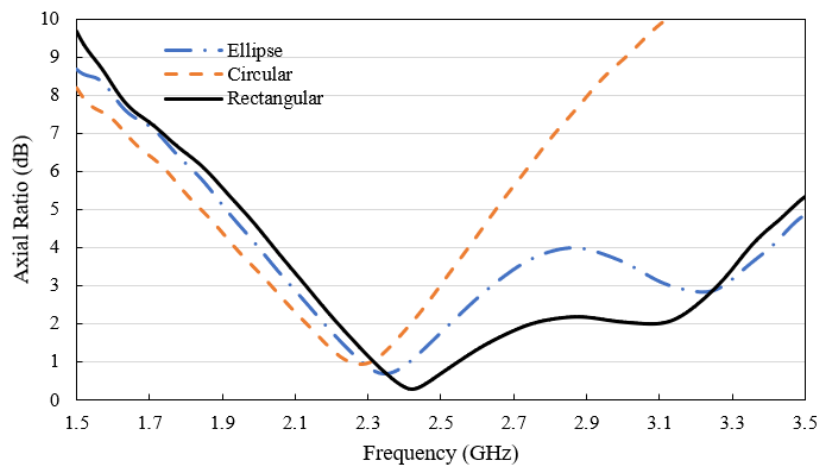

Figure 3.7. Comparison of 3 dB axial ratio bandwidth of the parasitic patch with an ellipse, a circular and a rectangular shape

Figure 3.7 shows a comparison of the 3 dB axial ratio of the three types of parasitic shape. An antenna with a circular-shaped parasitic generates narrower the 3 dB axial ratio bandwidth than ellipse shape. But an antenna with a rectangular-shaped parasitic generates a wider the 3-dB axial ratio bandwidth.

A parasitic or additional patch with rectangular-shaped on the circular-shaped slot was implemented to an antenna on step 1 to produce the new resonant frequency. Impact of the additional patch is as a new current line which correlates to the length of parasitic W_p, a width of the parasitic L_p and its position at the *x*-axis and *y*-axis. The impact of the width, length, and position on the y-axis and x-axis are analyzed and simulated. Figure 3.8 (a), Figure 3.8 (b), and Figure 3.8 (c) also Figure 3.8 (d) depict results of the simulation

by varying width, length, and position. Figure 3.8 (a) shows the influence of the parasitic width (W_p) varying from 0 mm, 20 mm, and 31 mm. This simulation is done with fixed other parameters with the parasitic length (L_p) of 12 mm placed on the x-axis (X_p) of 8-mm and y-axis (Y_p) of 5-mm. When the parasitic width of 0 mm, the antenna can reach the 3-dB axial ratio bandwidth of 270 MHz. When the parasitic width (W_p) of 20 mm, it produces the 3-dB axial ratio until 210 MHz and generates the gain to be lower of 3.47 dBic in the resonant frequency of 2.2 GHz. While the parasitic width (W_p) is extended until 31 mm, the antenna generates the 3 dB in two frequencies, in the lower frequency of 2.35 GHz and frequency of 3.44 GHz. The 3-dB axial ratio in lower frequency achieved of 360 MHz and in higher frequency achieved 160MHz. This design yields a gain of 3.6 dBic in 2.2 GHz as the resonant frequency. This simulation indicates when the width of a parasitic patch more than 31 mm, it generates better axial ratio bandwidth.

Figure 3.7 (b) depicts the impact of the parasitic length (L_p) from 2 mm, 6 mm and 12 mm. This simulation is done with fixed other parameters, the parasitic width (W_p) in 31mm placed on the x-axis (X_p) of 8 mm and y-axis (Y_p) of 5 mm. While the parasitic length (L_p) of 2 mm, this model generates two the circular frequency in 2.35 GHz and in 2.58 GHz, with the 3-dB bandwidth of 229 MHz on a lower frequency and 180 MHz on a higher frequency. While the patch length (L_p) of 6 mm, it generates the 3-dB axial ratio of 300 MHz and 220 MHz in frequency 2.37 GHz and 3.55 GHz. While the patch length (L_p) is extended till 12 mm, this design generates the 3dB axial ratio of 310 MHz and 250 MHz in the center frequency of 2.38 GHz and 3.49 GHz. Fortunately, the center frequency of the 3dB axial ratio is moved to be closer to each other and generate the gain until 4.1 dBic.

(a)

(b)
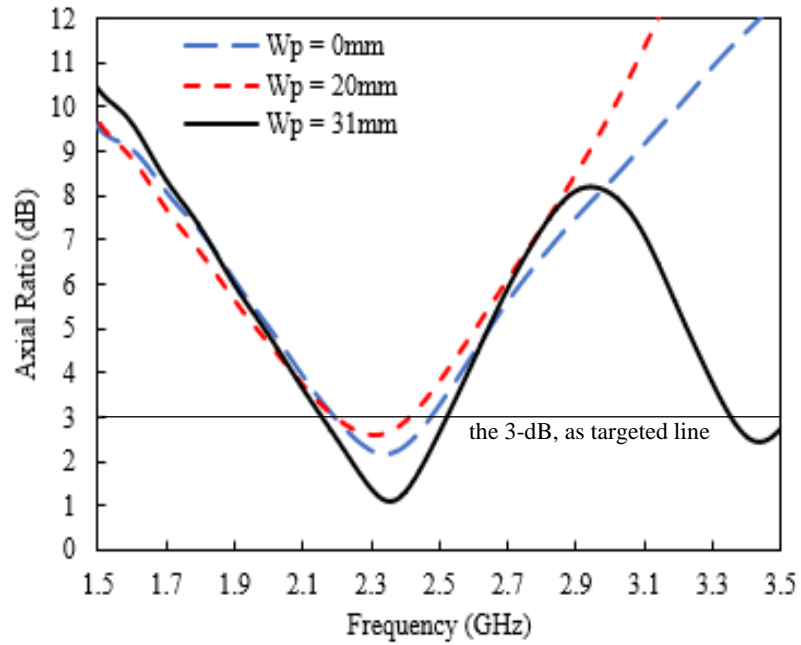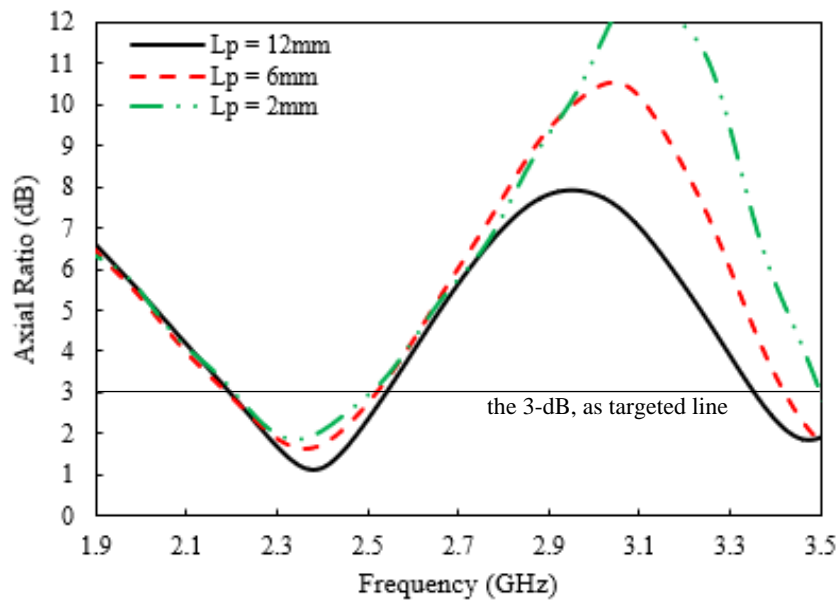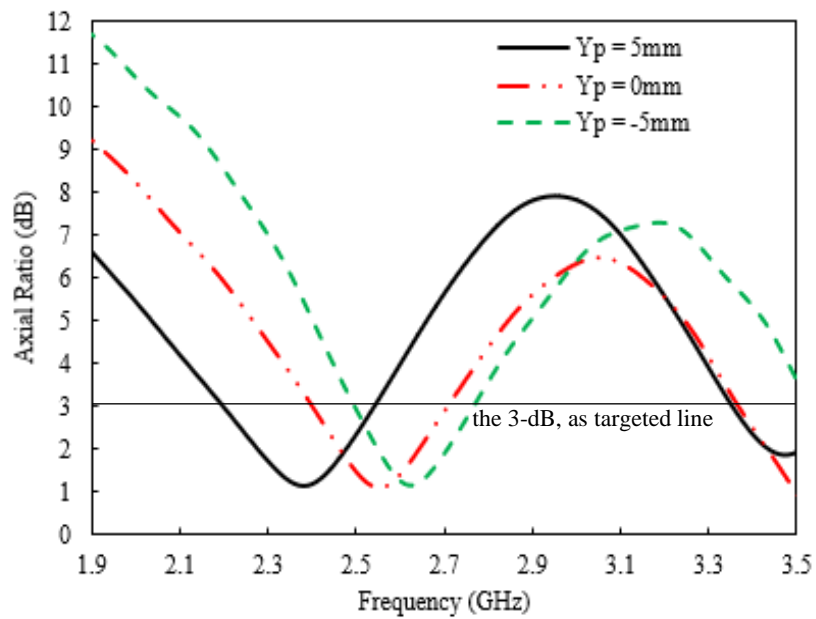
(c)
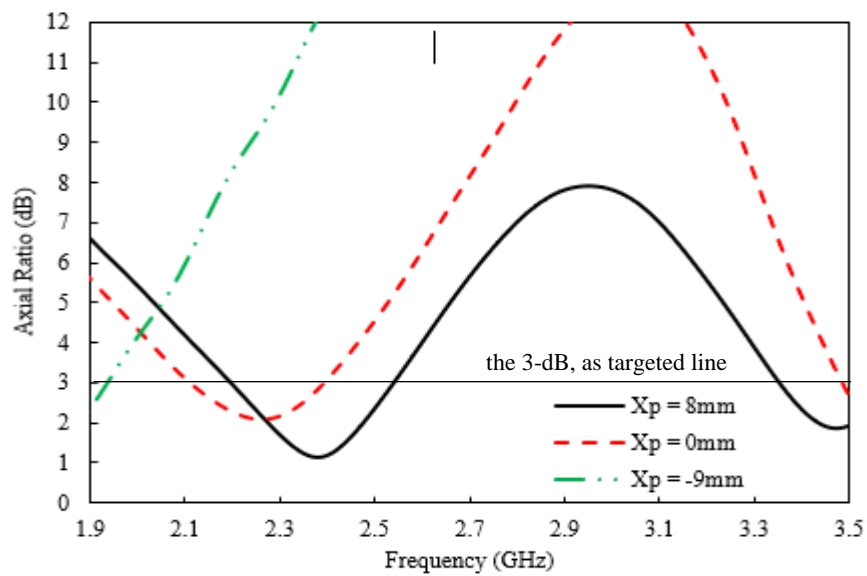
(d)

Figure 3. 8 The axial ratio results with the variation of (a). The parasitic length (L_p) (b). The parasitic width (W_p) (c). The parasitic point on the y-axis (Y_p) (d). The parasitic point on x-axis (X_p).

Figure 3.8(c) depicts the effect of the parasitic position on the y-axis (Y_p) varying from -5 mm, 0 mm, and 5 mm. The other parameters in this simulation are fixed with parasitic width (W_p) of 31 mm, (L_p) of 12 mm. While the center of the parasitic (Y_p) on -5 mm, it generates the 3-dB center frequency on 2.63 GHz and on 3.7 GHz. When the parasitic center Y_p of 0mm, it produces the 3-dB CF on 2.56 GHz and on 3.56 GHz. If the parasitic center (Y_p) placed on 5 mm, it generates the 3-dB on 2.39 GHz and on 3.45 GHz. Based on this simulation, it shows that the parasitic position on the y-axis (Y_p) sensitive to the center frequency of the 3-dB.

Figure 3.8(d) refers to the effect of the parasitic position on x-axis (X_p) on -9 mm, 0 mm, and 8 mm. This step makes others parameter in fix value, with the parasitic width (W_p) of 31 mm, the parasitic length (L_p) of 12 mm. While the parasitic center (X_p) placed on -9 mm, it generates the 3-dB center frequency bandwidth until 190 MHz. If the parasitic center X_p placed on 0 mm, it generates the 3-dB ARBW of 290 MHz in lower frequency and 190 MHz in higher frequency. If the parasitic center X_p of 8 mm, the 3-dB center frequency generates the 3-dB ARBW of 340MHz and 250MHz. The simulation result shows that the parasitic center X_p generate a higher frequency while its position on the positive x-axis.

However, a combination of slots having symmetrical length and a rectangular parasitic patch produces a narrow 3-dB ARBW. The next process is to extend the truncation length (L_{s1}) on the bottom side to be 48.79 mm and truncation length (L_{s2}) on the upside to be 40.79 mm. This unsymmetrical rectangular truncation can enhance the 3-dB axial ratio until 51.5 %, in the frequencies of 2.1 - 3.3 GHz. This design step generates higher gain until 4.71 dBic in 2.2 GHz. The maximum gain of this design is 4.8 dBic in 2.28 GHz. But this design has a weakness that the impedance frequency is moved to a higher frequency from 2.27 GHz until 3.32 GHz, and the deepest curve of the

reflection coefficient reaches -45 dB at 2.69 GHz. The frequency of impedance must be moved to a lower frequency around 2.2 GHz as an antenna requirement. A technique to overcome this weakness is by modifying the feedline width on the upside (W_{f2}) to be 10 mm, as depicted in figure 3.5. This design produces the bandwidth of impedance from 1.8 GHz until 2.7 GHz, the antenna gain up to 4.65 dBic. The 3-dB axial ratio is from 2.21 GHz to 3.26 GHz or equal to 51.52 %, the deepest curve of 0.28 dB at 2.4 GHz. The tuning of the feeding line is an important thing to obtain good results. Results of step 1 as model conventional, step 2 is depicted in figure 3.8 and its performances are shown in table 3.4. Figure 10 show the distribution of electric field in frequency 2.2 GHz of : 0 degrees, 90 degrees and 180 degrees.
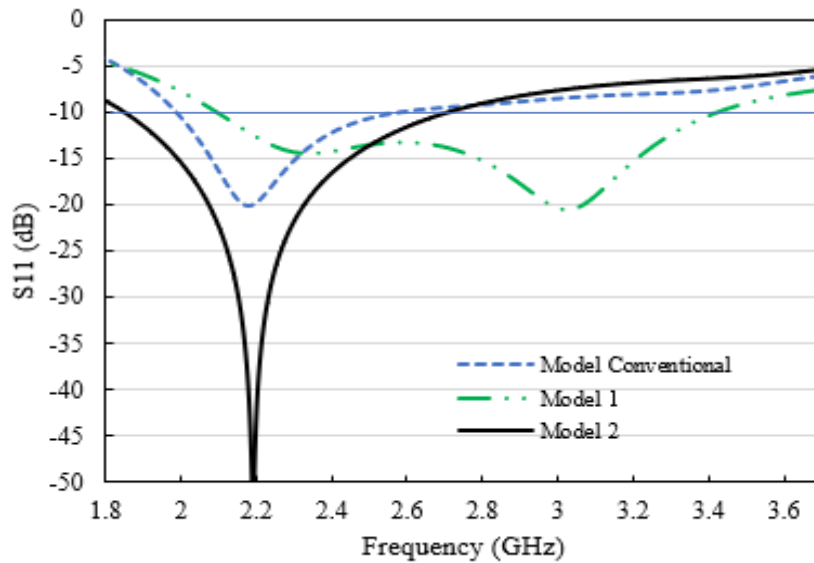
(a). S11
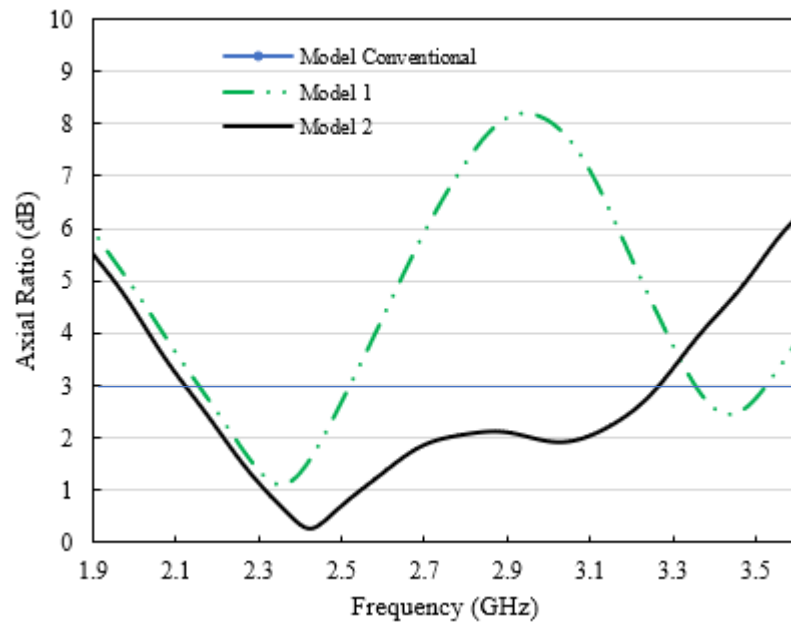
(b). Antenna Gain
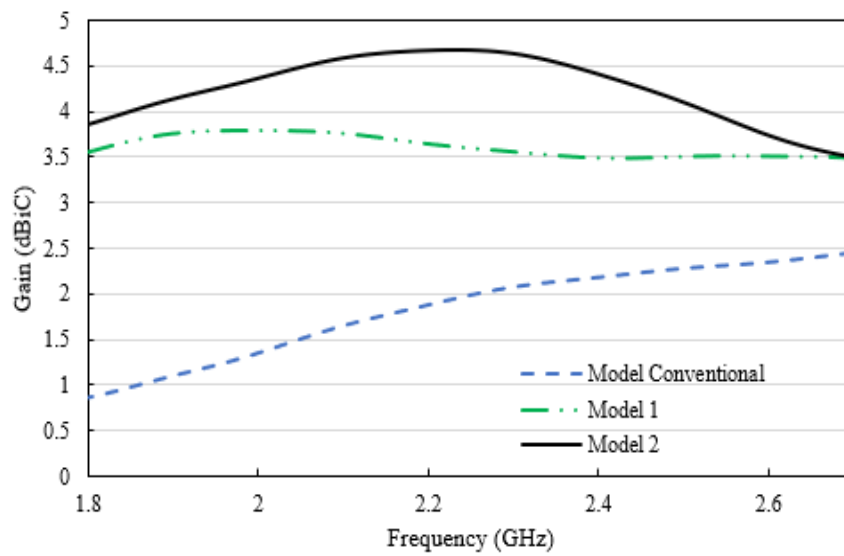
(c). Axial Ratio

Figure 3. 9. Results comparison of (a). S_{11} (b). Axial ratio (c). Antenna gains in step 1, step 2 of the antenna design

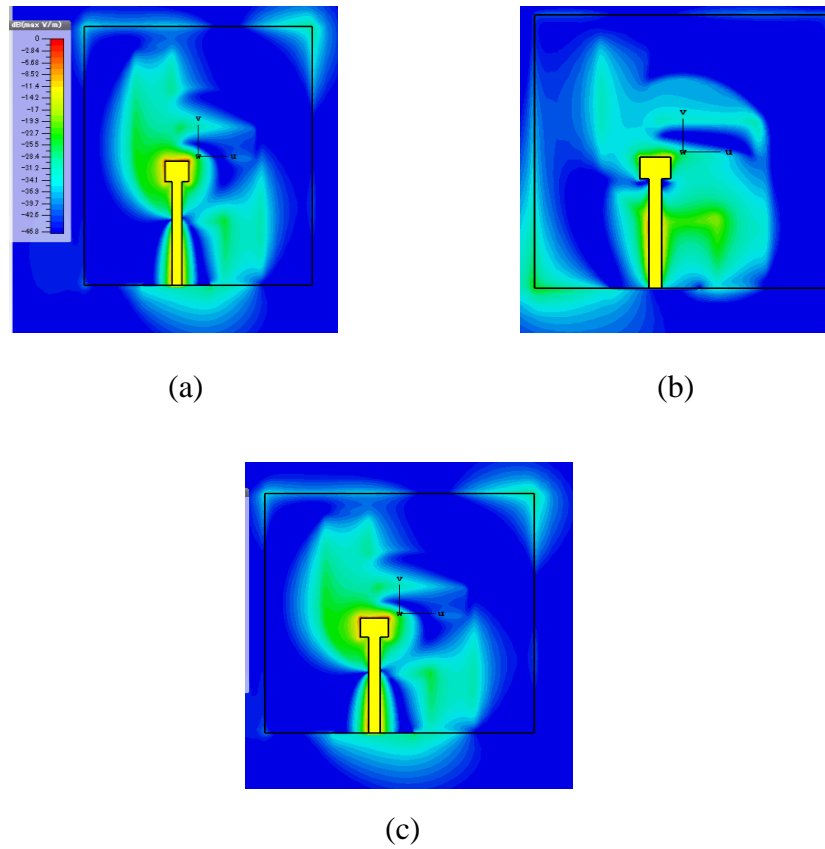(a)   (b)

(c)

Figure 3.10. Distribution of Electric field in frequency 2.2 GHz of :

(a) 0 degrees (b) 90 degrees and (c) 180 degrees

Table 3. 4 Simulation results of step 1, step 2 of the proposed antenna

Steps	$f_c$ibw (GHz)	Impedance Bandwidth (GHz)	$f_c$arbw (GHz)	3-dB ARBW (GHz), %	Gain (dBic)
Step 1	2.1789	1.9899-2.5839/ 27.26%	-	-	1.852
Step 2	3.0249	2.1009-3.4149/ 43.43%	2.36	2.16-2.52/ 15.25%	3.65
Step 3	2.1879	1.8489-2.7159/ 39.62%	2.42	2.13-3.26/ 46.69%	4.663

CHAPTER 4

4. EXPERIMENT AND MEASUREMENT

This chapter explains the steps of the experiment, the result of measurement, and discussion. The simulation results were compared to the measured results to know the antenna performance.

4.1 EXPERIMENT PROCESS

In Computer Simulation Technology (CST), the antenna was designed and simulated to analyses the best performance of the antenna. The next step is the fabrication of the antenna. To create an antenna layout for fabrication, DraftSight software such as Corel draw is needed to change the DXF file resulted from CST software. The photosensitive film is needed to copy the antenna layout on the front side and backside of a printed circuit board (PCB) by lightning with ultraviolet. Layout development and etching of the PCB employ chemical GEN-L and chemical EB-750 Etchant. The process of manufacturing the designed and simulated antenna by using chemicals is shown in Fig. 4.1.

Verification of the simulated results, both of the manufactured circular-slotted antennas are measured by using Network Analyzer, Agilent, E5062A. Measurement is done to take a value of antenna parameters such as the

reflectance coefficient (S11), the impedance, the 3 dB AR, the pattern, and the antenna gain.
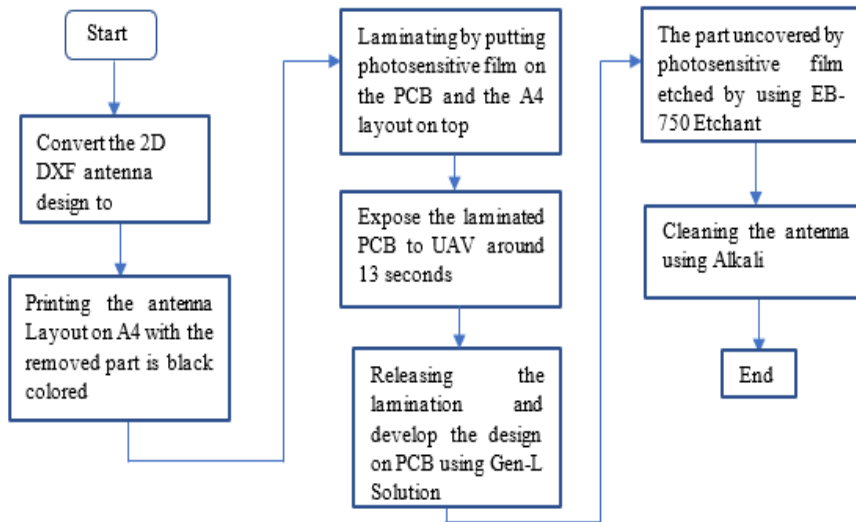

Figure 4. 1 Experimental process of antenna fabrication using PCB, Gen-L, EB-750, and Alkali.

The AR is measured by transmitting the fabricated antenna by two calibrated RHCP and LHCP tester antennas over the frequency interval. Port of the calibrated antenna is set to port 1 of the network analyzer, and the port of fabricated antenna is connected to port 2 of the vector network analyzer. The AR of the antenna is determined as Equation 4.0 below.

$$AR(dB) = 20 \, log \left[\frac{P_{RHCP} + P_{LHCP}}{P_{RHCP} - P_{LHCP}} \right] \qquad (4.0)$$

where,

P is measured power, and AR is the axial ratio of the antenna under test.

The antenna pattern was measured by illuminating the antenna with the LHCP and the RHCP-calibrated antenna at their *x-z* axis, *y-z* axis. The fabricated antenna is spun 360^0 from 0^0 to 359^0 to measure the electric field power for each angle point in one determined frequency. The configuration of antenna and VNA port is like the AR setup. Results for each frequency are LHCP and RHCP antenna pattern at *x-z*, *y-z* axes.

Measurement of antenna gain is set up by illuminating the fabricated antenna and a dipole antenna as a reference. A gain of the LHCP and RHCP antenna can be determined using the mathematic equation as below, Equation 4.1 and Equation 4.2.

$$G_{RHCP} \ (dBic) = (P_{RHCP}(dB) - \ P_{dipole} \ (dB) - 0.85 \qquad (4.1)$$

$$L_{RHCP} \ (dBic) = (P_{LHCP}(dB) - \ P_{dipole} \ (dB) - 0.85 \qquad (4.2)$$
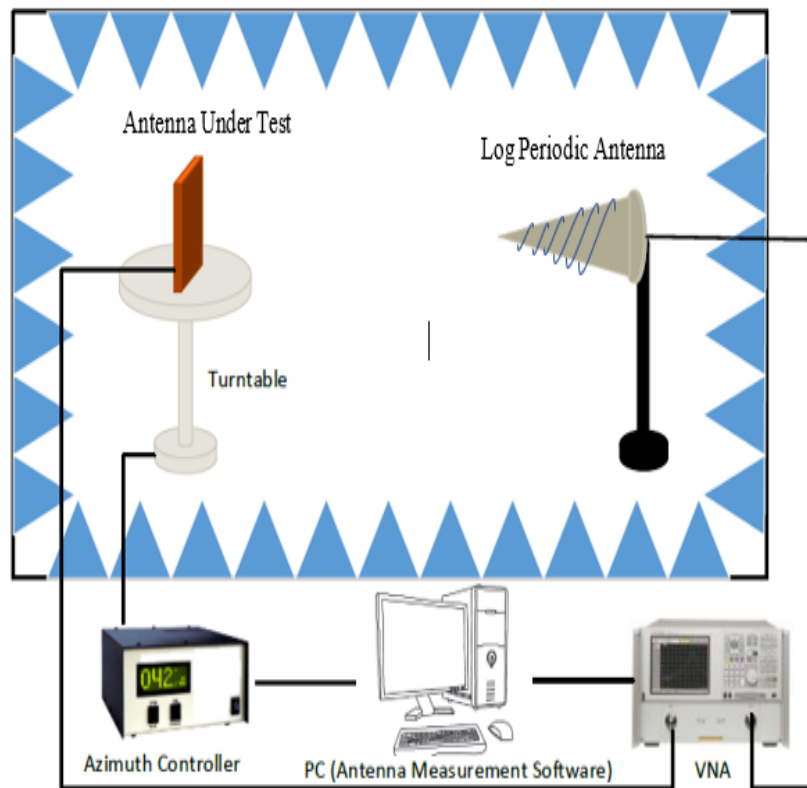
Figure 4. 2 Setup of antenna measurement: antenna, controller, PC, and network analyzer.

A gain of the fabricated antenna is G. Number of -0.85 is a result of a half-wave dipole antenna 2.15 dB, and gain correction of -3 dB, while CP antenna is compared to a dipole antenna. The experimental setup is illustrated in Fig. 4.2 for cable connection and Fig. 4.3 (a) for coefficient reflection, (b) for gain and axial ratio measurement.
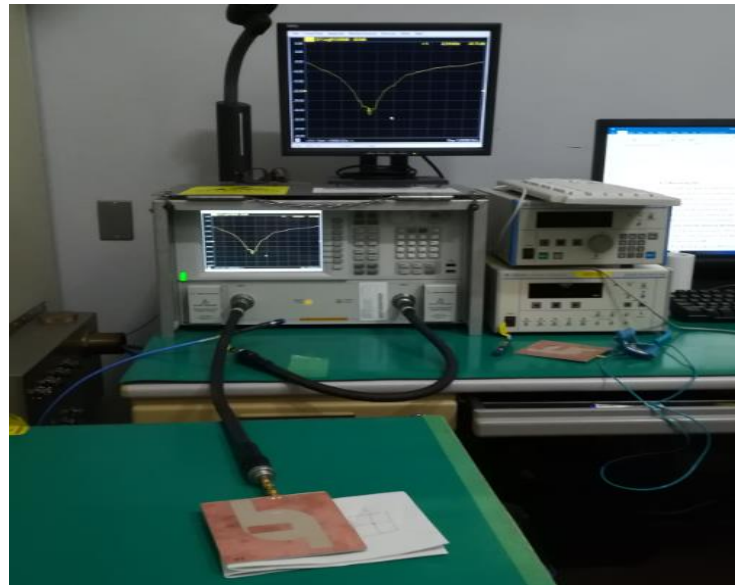
(a) Reflection Coefficient Measurement
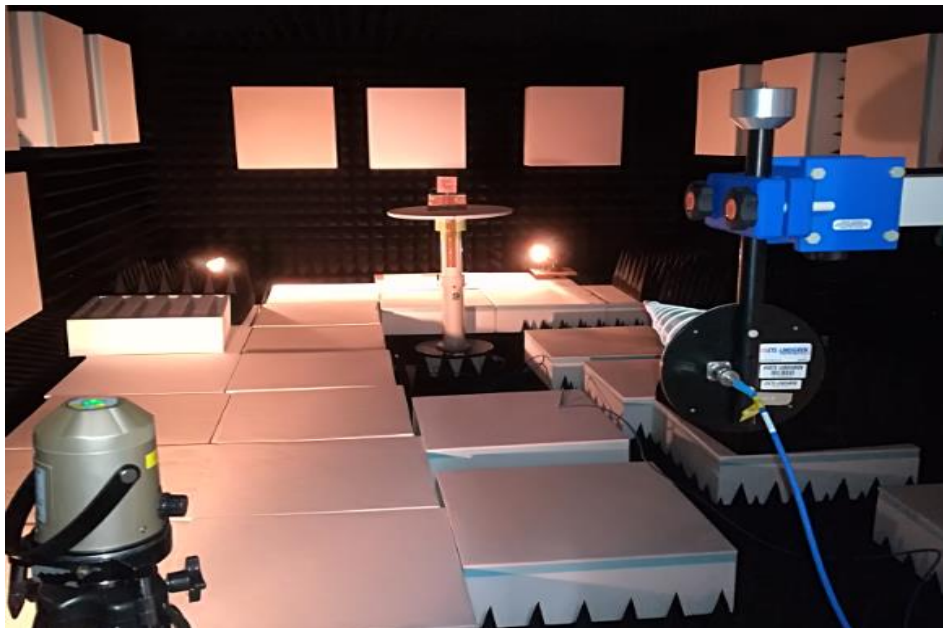
(b) Axial ratio dan Gain measurement

Figure 4. 3 (a) Reflection coefficient measurement, (b) Axial ratio, and gain
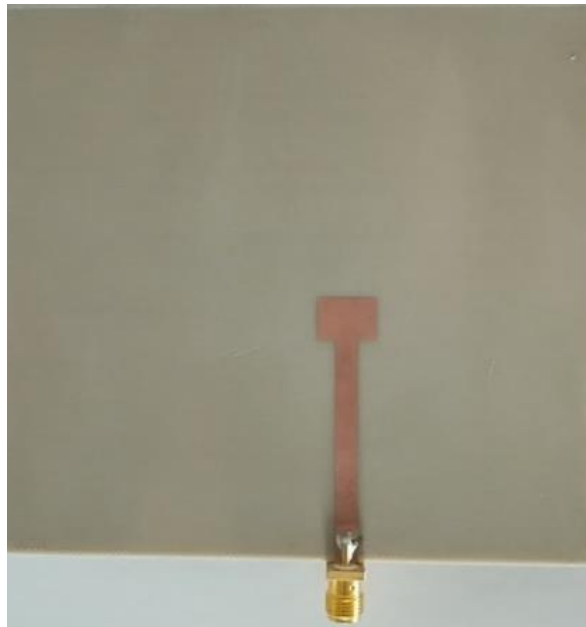measurement in an anechoic chamber.

4.2. RESULTS OF TYPE-1 ANTENNA

Photograph of type-1 fabricated antenna can be seen in Figure 4.4. Figure 4.5.a shows that the reflection coefficient of the simulation result compared with the measurement results shows good agreement, even though the deep of measured result better than the simulation result. The reflection coefficient of the measured antenna under 10 dB is 58% from 1.7 - 3 GHz. Fig. 4.5.b shows that the axial ratio of the simulation result compared with the measurement results shows good agreement. The measured 3-dB ARBW is 14.88% from 2.02 – 2.35 GHz. This type-1 fabricated antenna generates a left-handed circular polarization (LHCP). This antenna achieves a peak gain of 4.5 dBic at a frequency of 2.2 GHz, as shown in figure 4.5.c.
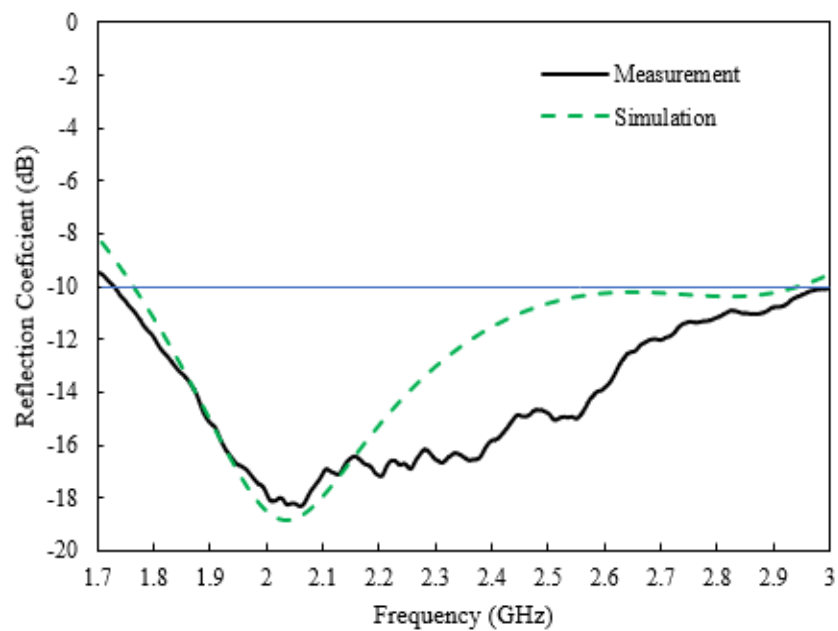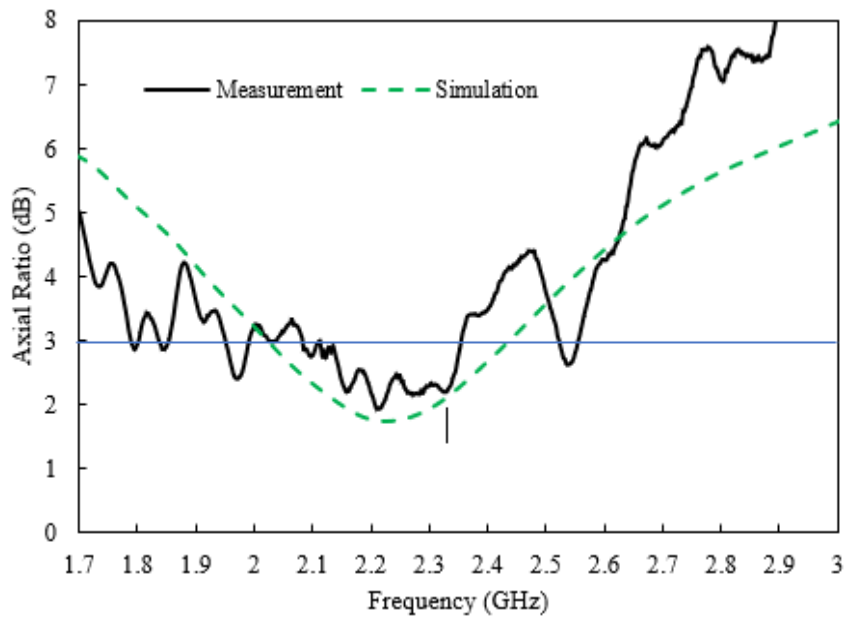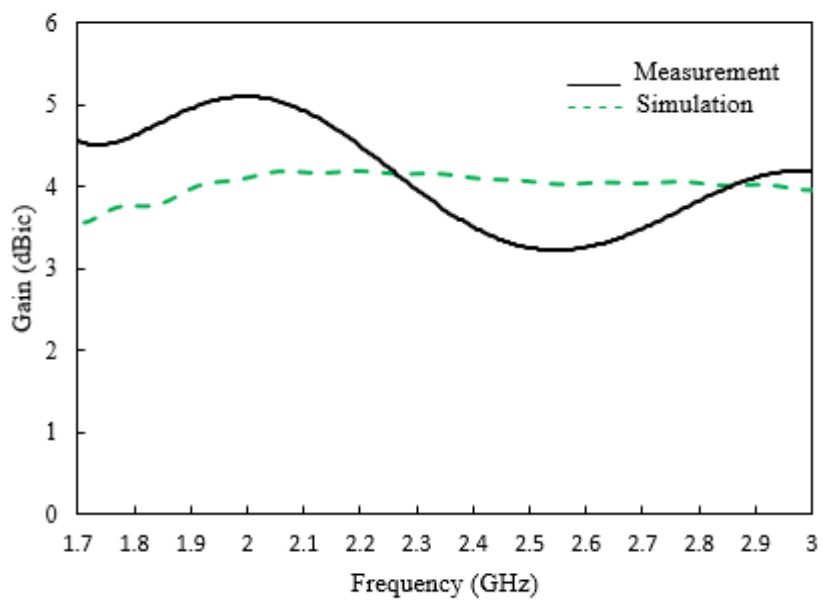

(a)

(b)

Figure 4. 4 Photograph of the type-1 manufactured antenna (a) front side as grounded-patch, (b) backside as a feeding line.

(a) Reflection coefficient (S_{11})

(b) Axial Ratio (AR)

(c) Gain

Figure 4. 5 Comparison of simulated and measured results of (a) S11, (b)

AR, (c) Gain of type-1 fabricated antenna.

4.3 RESULTS OF TYPE 2 ANTENNA

The design of antenna type-1 is modified to enhance the ARBW to be type 2 circularly-slotted antenna by added a parasitic patch. The performance must be tested to know the performance. Photograph of antenna type-2 can be seen in Fig. 4.6.
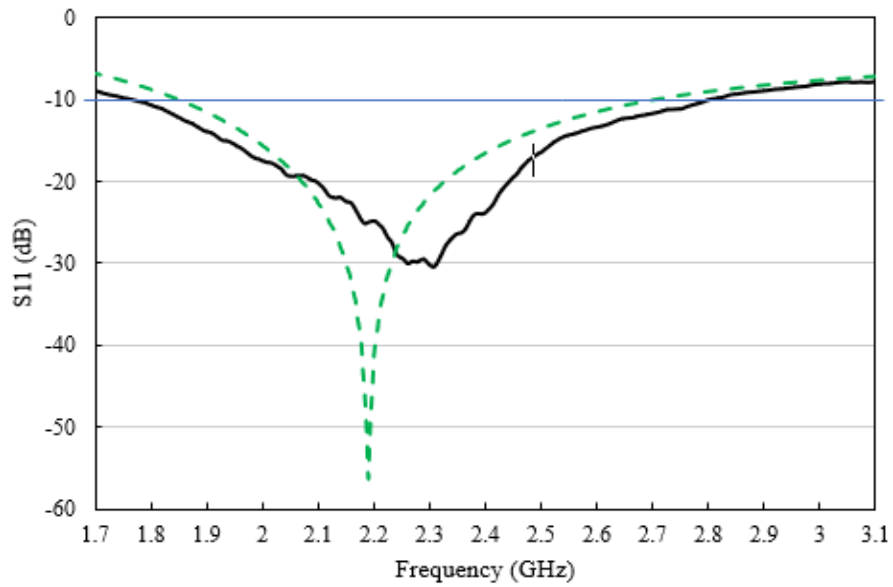

(a) Front side, as grounded-patch
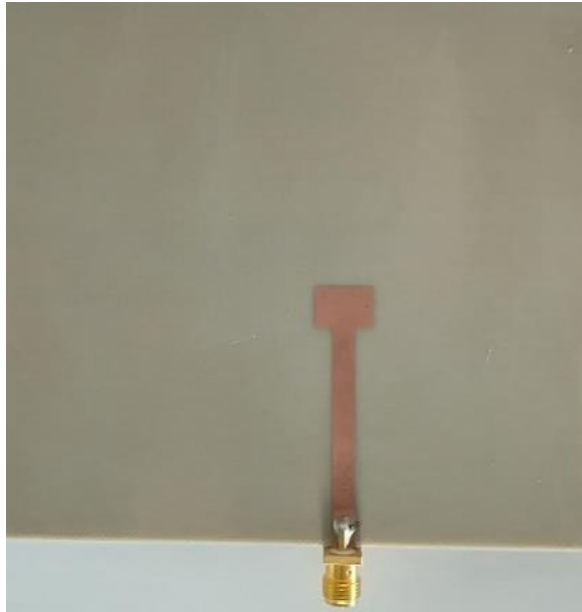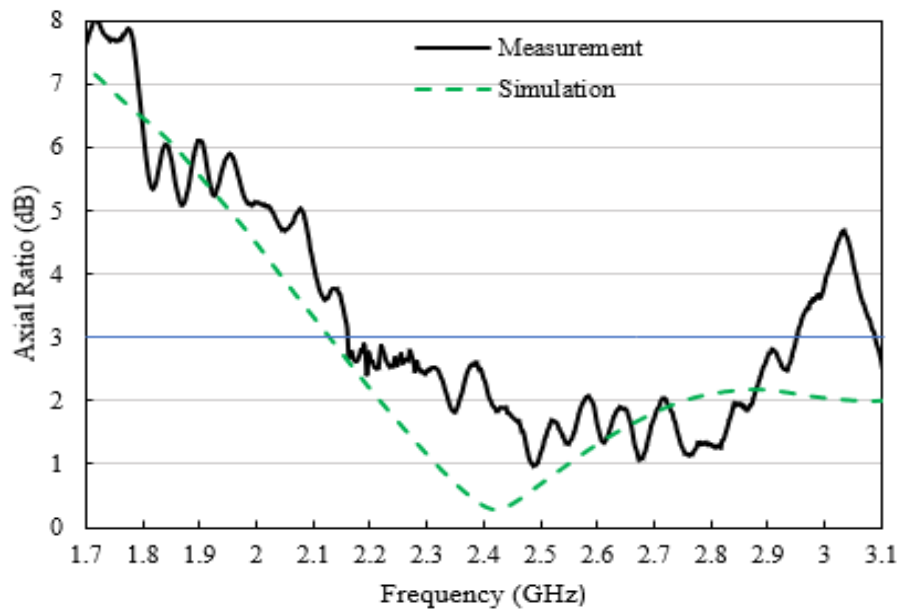
(b) Backside, as a feeding line

Figure 4. 6 (a) Front side as grounded-patch, (b) backside as a feeding line

The reflection coefficient of the fabricated antenna, as shown in Fig. 4.7.(a) is 862.5 MHz from 1.85 to 2.71 GHz. It presents a good agreement with the simulated result. The center of resonant frequency is shifted to a higher frequency from 2.2 GHz to be 2.3 GHz. The measured bandwidth is wider than the simulated one in lower frequency. The 3-dB ARBW of the fabricated antenna produces a bandwidth of 787.5 MHz, from an interval frequency of 2.1 to 2.95 GHz. The measured result is narrower than the simulation results as described in Figure 4.7(b). The frequency of the 3-dB AR is all inside of the reflection coefficient bandwidth. This confirms that the parasitic patch significantly enhances the axial ratio of type 1 circularly-slotted antenna.

(a) S11

(a) Axial Ratio (AR)

Figure 4. 7. Comparison of simulated and measured results of

(a) S11, (b) AR of type-2 antenna.

The antenna under test (AUT) is radiated with left-handed circular polarization and right-handed circular polarization waves at *x-z*, *y-z* axis. The fabricated antenna produces a bi-directional pattern with RHCP at $\theta = 180^0$ and LHCP at $\theta = 0^0$. Radiation patterns of far-field on *x-z*, *y-z* axis at 1.8 GHz, 2.2 GHz, 2.6 GHz are depicted in Figure 4.8.
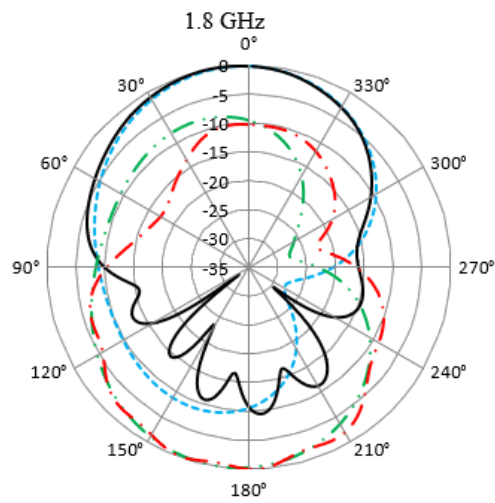
(a) 1.8 GHz
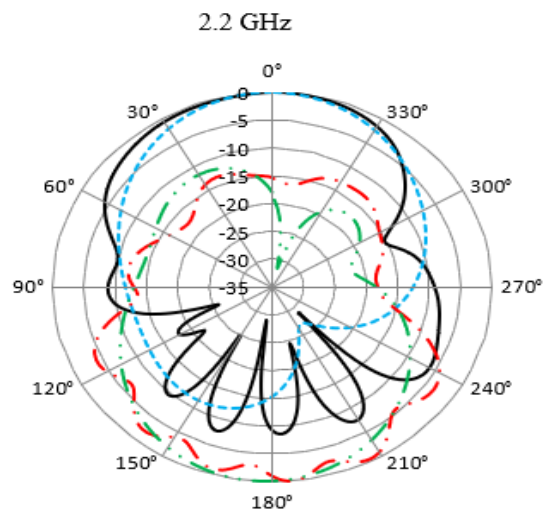
(b) 2.2 GHz
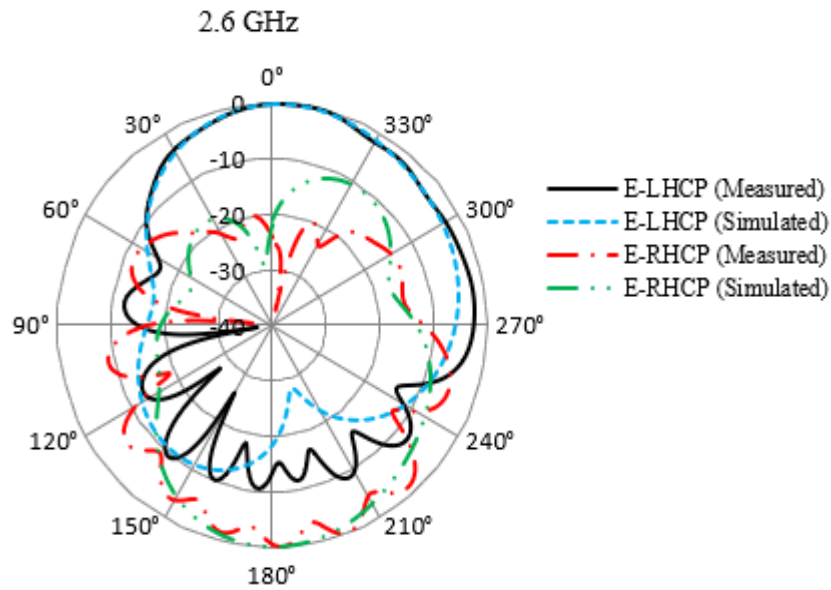
(c)

Figure 4. 8 Comparison of the measured and simulated radiation patterns on x-z axis at (a) 1.8 GHz, (b) 2.2 GHz, (c) 2.6 GHz

The measured radiation pattern in the frequency of 1.8 GHz, 2.2 GHz, and 2.6 GHz shows excellent consistency with the simulated results. This measured radiation pattern approves that the proposed antenna produces a circularly- polarized operation as predicted at the front and backside.

Figure 4. 9 Comparison of measured and simulated antenna gain

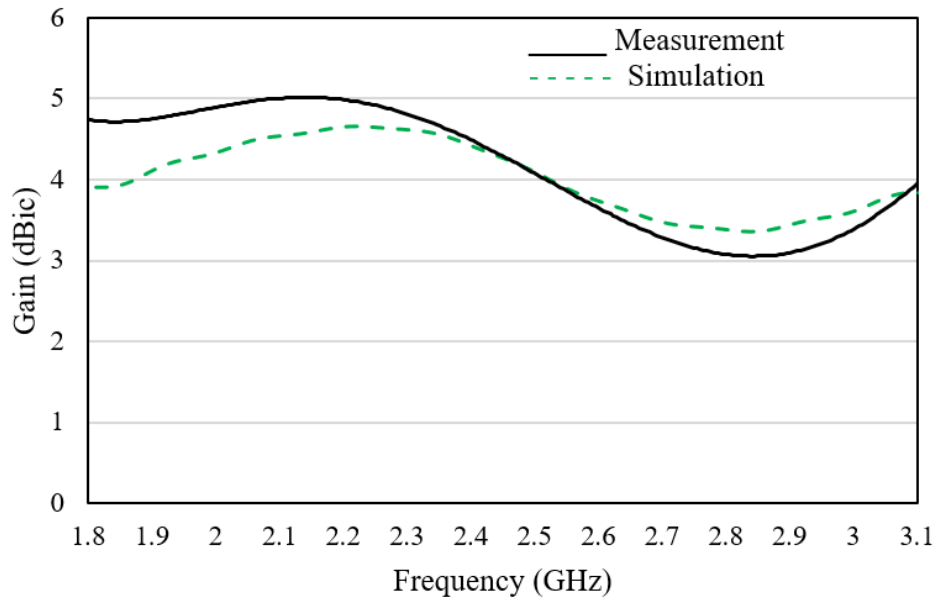Figure 4.9 depicts the measured and simulated results of LHCP gain. It produces an average gain of around 4 dBic. It is similar on 2.4 - 2.6 GHz to the simulated one, but higher gain at a frequency from 1.7 - 2.4 GHz and lower gain at a frequency under 4 dBic from 2.6 to 3.1 GHz.

CHAPTER 5

5. CONCLUSIONS AND NEXT WORK

5.1 CONCLUSIONS

The focus of this thesis is on study and design antenna for ionospheric research based on remote sensing satellite in 2.2 GHz and for its communication 2.5 GHz. The proposed antennas are circularly-polarized antennas by using a microstrip material installed onboard a small satellite. For this application, two types of circularly-polarized circular-slotted antennas were designed and developed.

The proposed antenna is simulated on CST software by determining antenna specification : the center frequency, minimum gain, bandwidth, pattern, size, polarization and compactness. Commonly, a higher frequency band is selected in order to make an antenna satisfying size requirements, especially for a small satellite. In previous beacon satellites, such as CERTO beacon using a crossed-yagi antenna in the frequency of 150 MHz and 400 MHz and Cosmic 2 using helix antenna in the frequency of 400 MHz, 965 MHz and 2200 MHz. But those antennas are not sufficient for small satellites caused relatively big size.

Circularly-polarized antennas are the best choice for satellites because of their strength to multi-path effects, polarization mismatch, and Faraday`s rotation effect. The Faraday`s rotation causes a spin of the polarization plane, that is proportional to the part of the magnetic field in the direction of wave propagation.

The first type of antenna is fabricated on a single substrate, with a substrate thickness of 1.6 mm. The antenna consists of a ground part on the front side

and a feeding line on the backside of the substrate. The antenna is designed with a square-shaped patch, with the size the length L of 100 mm, the width W of 100 mm, and a circularly-shaped slot is developed in the patch center with the radius r of 26.5 mm.

The antennas apply a linearly-polarized conventional type of the circularly-slotted antenna as a basic design. Modifications were done on the ground side by giving truncations and on the feedline by shifting and tuning the antenna to manage the antenna impedance.

The first type generates circularly-polarized wave radiation by implementing two rectangular truncations and a shifted feed line from its center. Improvement of the 3-dB ARBW, it requires setting the length of truncation. It can be approved that a pair of rectangular truncation has an important impact to enhance the 3-dB axial ratio bandwidth and the gain. This design is developed for only the beacon transmitter. The measured results of the antenna for beacon transmitter confirm of performance with impedance bandwidth of 58% from 1.7 - 3 GHz and CP bandwidth of 14.88 % in frequency 2.02 – 2.35 GHz. The antenna gain can reach 4.5 dBic at 2.2 GHz.

The second type of antenna is fabricated on a single substrate, with a substrate thickness of 1.6 mm. The antenna consists of a ground part on the front side and a feeding line on the backside of the substrate. The antenna is designed with a square-shaped patch, with the size, the length L of 100 mm, the width W of 95 mm and a circularly-shaped slot is developed in the patch center with the radius r of 26.5 mm.

The second type antenna uses the design of the first type with an additional parasitic patch on the circularly-shape slot. The shape of parasitic is very critical to the 3-dB axial ratio bandwidth enhancement. In the simulation process, by using three types of parasitic shapes such as a circularly-shape parasitic, an elliptically-shape parasitic, a rectangularly-shape parasitic, the rectangularly-shape parasitic can generate a wider 3-dB ARBW. The

simulated and fabricated antenna successfully enhances the 3-dB ARBW of 35.7% and the maximum gain of 5 dBic. Both of this fabricated antenna is developed for a beacon transmitter in 2.2 GHz with a bandwidth of 40 MHz and communication in 2.5 GHz with BW of 100 MHz. Both of the proposed antennas, type one and type 2, have bi-directional radiation patterns.

Finally, the designed antenna can be used to wideband circularly-polarized antenna applications for small satellites for beacon transmitter, communication, and other applications.

5.2 CONTRIBUTIONS

This thesis makes contributions of the axial ratio and gain enhancement for nanosatellite using a parasitic patch on microstrip CSA.

The contributions offered in this thesis on the microstrip antenna are concluded as follows:

- A novel method to generate circularly polarized (CP) wave in L band with center frequency in 2.2 GHz by making use of a pair of unsymmetrical rectangular truncation on the centered-circular slot.

- A novel method is to broaden the CP bandwidth of a CSA antenna for beacon frequency in 2.2 GHz with a bandwidth of 40 MHz and data communication 2.5 GHz with a bandwidth of 100 MHz. This antenna design is making use of a pair of the unsymmetrical rectangular truncation incorporated with parasitic path and shifted feedline.

- Measured and simulated results indicate good consistency of the fabricated antennas.

5.3 NEXT WORKS

The research in this dissertation may be continued for the next research, such as listed below :

1.   Design and development of an antenna with higher CP antenna gain.
2.   Development of a CSA array for antenna beacon receiver on the ground to obtain improved gain.
3.   To test the performance of the fabricated antenna for beacon signal transmission and data transmission simultaneously in a single frequency.

Bibliography

[1] J. T. S. Sumantyo, N. Imura, "Development of GNSS-RO and EDTP sensors onboard microsatellite for ionosphere monitoring," in IGARSS, pp. 4886-4889, IEEE, 2015.

[2] P. P. Sitompul, J. T. S. Sumantyo, F. Kurniawan, C. E. Santosa, T. Manik, A. Awaludin, M. Y. Chua, "Dual-band Circularly-polarized Microstrip Antenna for Nano Satellite," PIERS, Toyama, Japan, 2018.

[3] N. L. Yen, C. J. Fong, C. H. Chu, J. J. Miau, Y. A. Liou, and Y. H. Kuo, "Global GNSS Radio Occultation Mission for Meteorology, Ionosphere & Climate," Chapter. DOI: 10.5772/6928, January 2010

[4] P. A. Bernhardt., C. L. Siefring, "New satellite-based systems for ionospheric tomography and scintillation region imaging," Radio Science, Vol. 41, RS5S23, 2006.

[5] M. Yamamoto, "Digital beacon receiver for ionospheric TEC measurement developed with GNU Radio," Earth Planets Space, 60, 2008.

[6] P. A. Bernhardt, C. L. Siefring, I. J. Galysh, T. F. Rodilosso, D. E. Koch, T. L. MacDonald, M. R. Wilkens, G. P. Landis, "Ionospheric applications of the scintillation and tomography receiver in space (CITRIS) mission when used with the DORIS radio beacon network," J Geod, 80: 473–485, 2006

[7] Y. V. Yasyukevich, A. A. Mylnikova, V. B. Ivanov, "Estimating the Absolute Total Electron Content Based on Single Frequency Satellite Radio Navigation GPS/GLONASS Data," Solar-Terrestrial Physics, Vol. 3. Iss. 1, pp. 128–137, 2017.

[8]   R. Nugent, R. Munakata, A. Chin, R. Coelho, J. P. Suari, "The CubeSat: The Picosatellite Standard for Research and Education," AIAA SPACE 2008 Conference & Exposition, September 2008, San Diego, California

[9]   D. D. Corso, C. Passerone, L. Reyneri, C Sansoe, S. Speretta, M. Tranchero, "Design of a University Nano-Satellite : the PiCPoT Case," IEEE Transactions on Aerospace and Electronic Systems Vol. 47, No. 3 July 2011.

[10]   K. L. Wong, C. Huang, W. S. Chen, "Printed Ring Slot Antenna for Circular Polarization", IEEE TAP, Vol. 50, No. 1, 2002.

[11]   J. Y. Sze, C. I. G. Hsu, M. H. Ho, Y. H. Ou, M. T. Wu, "Design of Circularly Polarized Annular-Ring Slot Antennas Fed by a Double-Bent Microstripline", IEEE Transactions on Antennas and Propagation, Vol. 55, No. 11, November 2007.

[12]   M. H. Rees, "Physics and chemistry of the upper atmosphere" Cambridge University Press.

[13]   R. G. Burnside, J. C. Walker, R. A. Behnke, C. A. Gonzales, "Polarization electric fields in the nighttime F layer at Arecibo". J Geophys Res, 88: 6259–6266, 1983.

[14]   O. D. L. Beaujardière, L. Jeong, B. Basu, S. Basu, T. Beach, P. Bernhardt, W. Burke, K. Grove, R. Heelis, R. Holzworth, C. Huang, D. Hunton, M. Kelley, R. Pfaff, J. Retterer, F. Rich, M. Starks, P. Straus, C. Valladares, "C/NOFS : a mission to forecast scintillations,". J Atmos Solar-Terr Phys 66:1573–1591, 2004.

[15]   Y. Zou, "Ionospheric scintillations at Guilin detected by GPS ground-based and radio occultation observations", ASR 47, 945–965, 2011.

[16]   IPS Radio and Space Service, "Introduction to HF Radio Propagation,"

[17]   R. Leitinger, G. K. Hartmann, F. J. Lohmar, E. Putz, "Electron content measurements with geodetic Doppler receivers," Radio Science, Volume 19, Number 3, Pages 789-797, 1984.

[18]   H. Rishbeth and O. K. Garriott, "Introduction to Ionospheric Physics, New York, Academic Press", 1969.

[19]   D. Ouzounov, S. Pulinets, A. Romanov, A. Romanov, K. Tsybulya, D. Davidenko, M. Kafatos and P. Taylor, "Atmosphere-ionosphere response to the $M9$ Tohoku earthquake revealed by multi-instrument space-borne and ground observations: Preliminary results, Earthq Sci 24: 557–564, 2011.

[20]   T. Xu, Y. Hua, H. Zhang, Z. Chen, J. Wua, Z. Xu, "Ionospheric disturbances on 8 September 2010 : Was it connected with the incoming moderate Chongqing earthquake?", Advances in Space Research 50, 205–210, 2012.

[21]   T. Manik, M. Batubara, M. Latief, P. Sitompul, Y. Rubianto, M. Yamamoto, "Penggunaan Data TEC Suar Satelit dari Pengamatan GRBR Berbasis Kampanye untuk Tomografi Ionosfer di atas Jawa Barat Indonesia,"   In English "The use of Satellite Beacon TEC data from GRBR campaign-based observations for Ionospheric Tomography over West Java Indonesia," Jurnal Sains Dirgantara Vol. 15 No. 2 Juni 2018 : 85-98

[22]   Z. H. Ding, J. Wu, Z. W. Xu, B. Xu, L. D. Dai, "The Qujing Incoherent Scatter Radar : System Description and Preliminary Measurements," Ding et al. Earth, Planets and Space 70-87, 2018.

[23]   J. C. Juang, S. H. Ma, C. T. Lin, "Study of GNSS-R Techniques for FORMOSAT Mission," IEEE Journal of Selected Topics in Applied Earth Observations and Remote Sensing, Vol. 9, No. 10, October 2016.

[24]   T. W. Garner, T. L. Gaussiran, B. W. Tolman, R. B. Harris, R. S. Calfas, H. Gallagher, "Total electron content measurements in ionospheric physics," A. S. Research 42, 720–726, 2008.

[25] S. Jin, O. F. Luo, P. Park, "GPS observations of the ionospheric F2-layer behavior during the 20th November 2003 geomagnetic storm over South Korea," J Geod 82 : 883–892, 2008.

[26] A. D. S. Curiel, M. Lambert, D. Liddle, M. Sweeting, C. H. Chu, C. J Fong, G. C. Chang, "Introduction to Formosat-7/Cosmic-2 Mission", Conference on Small Satellite, 2013.

[27] J. T. S. Sumantyo, "Development of Microsatellites for Atmospheric and Land Deformation Observation," In Proceedings of the Asia Oceania Geoscience Symposium (AOGS), Hokkaido, Japan, August 2014.

[28] C. K. Pang, A. Kumar, C. H. Goh, C. V. Le, "Nano-Satellite Swarm for SAR Applications: Design and Robust Scheduling," IEEE Transactions on Aerospace and Electronic Systems Vol. 51, No. 2 April 2015.

[29] C. S. Ruf, S. Gleason, Z. Jelenak, S. Katzberg, A. Ridley, R. Rose, J. Scherrer, and V. Zavorotny, "The CYGNSS Nanosatellite Constellation Hurricane Mission", IGARSS 2012.

[30] P. P. Sitompul, J. T. S. Sumantyo, F. Kurniawan, and M. Nasucha, "Axial Ratio and Gain Enhancement of a Circular-Ring Slot Antenna Using a Pair of Asymmetrical Rectangular Slots and a Parasitic Patch for a Radio Beacon on a Nanosatellite," Aerospace, MDPI, 6, 39, 2019.

[31] C. A. Balanis, "Antenna Theory Analysis and Design," A John Wiley and Sons, Inc.

[32] T. J. Mizuno, J. D. Roque, B. T. Murakami, L. K. Yoneshige, G. S. Shiroma, R. Y. Miyamoto, and W. A. Shiroma, "Antennas for Distributed Nanosatellite Networks," IEEE, 2005.

[33] A. H. Lokman, P. J. Soh, S. N. Azemi, H. Lago, S. K. Podilchak, S. Chalermwisutkul, M. F. Jamlos, A. A. Al-Hadi, P. Akkaraekthalin, and S. Gao, "A Review of Antennas for Picosatellite Applications,"

Hindawi International Journal of Antennas and Propagation Volume 2017.

[34] S. Gao, Q. Luo, and F. Zhu, "Circularly Polarized Antennas," Wiley, IEEE.

[35] B.T. Strojny and R.G. Rojas, "Bifilar Helix GNSS Antenna for Unmanned Aerial Vehicle Applications," Antennas and Wireless Propagation Letters, IEEE, Vol. 13, page 1164-1167, 2014.

[36] J.Y. Sze and W.H. Chen, "Axial Ratio Bandwidth Enhancement of a Microstrip-Line-Fed Circularly Polarized Annular-Ring Slot Antenna," IEEE Transactions on Antennas and Propagation, vol. 59, no. 7, pp. 2450-2456, 2011.

[37] W. A. Imbriale, S. Gao, and L. Boccia, "Space Antenna Handbook," John Wiley and Sons, May 2010.

[38] C. Sun, H. Zheng, Y. Liu, "Compact dual-band circularly polarized GNSS antenna," Electronics Letters, Vol. 51, No. 20, Page 1559-1560, 2015.

[39] K. Hussein, "Conical linear spiral antenna for tracking, telemetry and command of low earth orbit satellites," PIER C, Vol. 29, Page 97-107, 2012.

[40] Gonzalez, J. Gmez, A. Tayebi, and F. Ctedra, "Optimization of a Dual-Band Helical Antenna for TTC Applications at S Band," Antennas and Propagation Magazine, IEEE, Vol. 54, No. 4, Page 63-77, 2012.

[41] K. Hussein, "Conical linear spiral antenna for tracking, telemetry and command of low earth orbit satellites," PIER C, vol. 29, pp. 97-107, 2012.

[42] E. Choi, J. Lee, T. Lee, and W. Lee, "Circularly Polarized S-Band Satellite Antenna with Parasitic Elements and Its Arrays," Antennas and Wireless Propagation Letters, IEEE, Vol. 13, Page. 1689-1692, 2014.

[43] J. Row and S. Wu, "Circularly-polarized wide slot antenna loaded with a parasitic patch," IEEE TAP, Vol. 56, No. 9, Page. 2826-2832, 2008.

[44] Nasimuddin, Z. Chen, and X. Qing, "Symmetric Aperture Antenna for Broadband Circular Polarization," IEEE TAP, Vol. 59, No. 10, pages. 3932-3936, 2011.

[45] N. Felegari, J. Nourinia, C. Ghobadi, and J. Pourahmadazar, "Broadband CPW-Fed Circularly Polarized Square Slot Antenna with Three Inverted-L-Shape Grounded Strips," IEEE Antennas and Wireless Propagation Letters, vol. 10, pp. 274-277, 2011.

[46] P. Rassamimut, P. Chuwong, and P. Ravipat, "Design of a dual-band quadrifilar helical antenna for radio beacon receiver," Symposium on Intelligent Signal Processsing and Communication Systems, December, 2011.

[47] M. Matsunaga, "A dual-band circularly polarized microstrip patch antenna with a cross shaped slot for 0.92/2.45 GHz RFID applications," IEICE Communications Express, Vol.1, 1–6, 2017.

[48] Sze, J.Y., Hsu, C. Chen, Chang, C. C. "Broadband CPW-fed circularly polarized square slot antenna with lightening-shaped feed-line and inverted-L grounded strips," IEEE Trans. Antennas Propag. 2010, 58, 973–977.

[49] C. J. Wang, C. H. Chen "CPW-Fed Stair-Shaped Slot Antennas with Circular Polarization", IEEE TAP, vol 57, No 8, 2009.

[50] Row, J. S. "The design of a squarer-ring slot antenna for circular polarization," TAP, IEEE, 53, 1967–1972, 2015.

[51] K. L. Wong, J. Y. Wu, C. K. Wu, "A circularly polarized patch loaded square slot antenna," Microwave Optical Technology Letters. 23, 363–365, 1999.

[52] L. Y. Tseng, T.Y. Han. "Microstrip-fed circular slot antenna for circular polarization," Microwave Optical Technology Letters, 50, 1056–1058, 2008.

[53] X. M. Qing, Y.W. M. Chia, "Circularly polarized circular ring slot antenna fed by stripline hybrid coupler, " Electron Letters, 35, 2154–2155, 1999.

[54] J. L. Zhang, X, Q Yang, "Integrated compact circular polarization annular ring slot antenna design for RFID reader," Progress Electromagnetism Res. Letter, 39, 133–140, 2013.

[55] T. N. Chang, J.M. Lin, "Circularly polarized antenna having two linked slot-rings," TAP, IEEE, 59, 3057–3060, 2011.

[56] M. Z. Aziz; Mufit, N. A Mufit, M. K. A. Rahim; M. R. Kamaruddin, "Design X-circular polarized with slant rectangular slot by using single port," In Proceedings of the 2012 International Symposium on Antennas and Propagation, Nagoys, Japan, 29 October–2 November 2012; pp. 555–558.

[57] H. J. Lu, C. L. Tang, K. L. Wong, "Single-feed slotted equilateral-triangular microstrip antenna for circular polarization," IEEE TAP, 47, 1174–1178, 1999.

[58] Peberlin P. S, Josaphat T. S. S., Farohaji K., Cahya Edi Santosa, Timbul Manik, Katsumi Hattori, Steven Gao, and Jann-Yenq Liu, "A Circularly Polarized Circularly-Slotted-Patch Antenna with Two Asymmetrical

Rectangular Truncations for Nanosatellite Antenna," Progress In Electromagnetics Research C, Vol. 90, 225–236, 2019.

[59] K. L. Wong, and J. Y. Wu, "Single-feed small circularly polarized square microstrip antenna," Electron Letter, Vol. 33, 1833–1834, 1997.

[60] F. Kurniawan, J. T. S. Sumantyo, G S. P, and A. Munir, "Wide bandwidth left-handed circularly polarized printed antenna with crescent slot," 2017 Progress In Electromagnetics Research Symposium - Spring (PIERS), 1047–1050, Russia, 2017.

Appendix 1 – Publications List

1.1. Peer-reviewed Journal Papers

<u>Peberlin Parulian Sitompul</u>, Josaphat T. Sri Sumantyo, Farohaji Kurniawan, Cahya Edi Santosa, Timbul Manik, Katsumi Hattori, Steven Gao, and Jann-Yenq Liu, "A Circularly Polarized Circularly-Slotted-Patch Antenna with Two Asymmetrical Rectangular Truncations for Nanosatellite Antenna," Progress In Electromagnetics Research C, Vol. 90, pp.225–236, 5 March 2019.

<u>Peberlin Parulian Sitompul</u>, Josaphat Tetuko Sri Sumantyo, Farohaji Kurniawan and Mohammad Nasucha, "Axial Ratio and Gain Enhancement of a Circular-Ring Slot Antenna Using a Pair of Asymmetrical Rectangular Slots and a Parasitic Patch for a Radio Beacon on a Nanosatellite," Aerospace MDPI, Vol.6, 39, 28 March 2019.

Agus Hendra Wahyudi, Farohaji Kurniawan, <u>Peberlin Parulian Sitompul</u>, and Josaphat Tetuko Sri Sumantyo, "Wideband LHCP 3D Printed Pyramidal Horn Antenna with Poisson Distribution Profile Polarizer for CP-SAR Sensor Onboard Microsatellite," Journal of Instrumentation, Automation and Systems, Vol.4, No.1, pp.10-14, UnsysDigital, March 2019.

Chua Ming Yam, Josaphat Tetuko Sri Sumantyo, Cahya Edi Santosa, Good Fried Panggabean, Franciskus D. Sri Sumantyo, Tomoro Watanabe, Ya Qi Ji, <u>Peberlin Parulian Sitompul</u>,

Mohammad Nasucha, Farohaji Kurniawan, Babag Purbantoro, Asif Awaludin, Karna Sasmita, Eko Tjipto Rahardjo, Gunawan Wibisono, Retnadi H. Jatmiko, Sudaryatno, Taufik H. Purwanto, Barandi S. Widartono, and Muhammad Kamal, "The Maiden Flight of Hinotori-C: The First C Band Full Polarimetric Circularly Polarized Synthetic Aperture Radar in the World," IEEE Aerospace and Electronic Systems Magazine, Vol.34, No.2, pp.24-35, February 2019 DOI. No. 10.1109/MAES.2019.180120.

Mohammad Nasucha, Josaphat Tetuko Sri Sumantyo, Cahya Edi Santosa, Peberlin Parulian Sitompul, Agus Hendra Wahyudi, Yang Yu, and Joko Widodo, "Computation and Experiment on Linearly and Circularly Polarized Electromagnetic Wave Backscattering by Corner Reflectors in an Anechoic Chamber ," Computation, Vol.7, No. 4, pp. 55-, MDPI, 24 September 2019, 10.3390/computation7040055

1.2 Conference Papers

Farohaji Kurniawan, J. T. S. Sumantyo, P. P. Sitompul, G. S. Prabowo, A. Aribowo, and A. Bintoro, "Comparison Design of X-band Microstrip Antenna for SAR Application", Innovative Microwave Remote Sensing, 2P1, Progress in Electromagnetics Research Symposiums (PIERS 2018), 1-4 August 2018, Toyama.

P. P. Sitompul, J. T. S. Sumantyo, F. Kurniawan, C. E. Santosa, T. Manik, A. Awaludin, and M. Y. Chua, "Dual-band Circularly-polarized Microstrip Antenna for Nano Satellite," Innovative

Microwave Remote Sensing, 2P1, Progress in Electromagnetics Research Symposiums (PIERS 2018), 1-4 August 2018, Toyama.

Ming Yam Chua, Josaphat Tetuko Sri Sumantyo, C. E. Santosa, G. F. Panggabean, Ya Qi Ji, <u>P. P. Sitompul</u>, and M. Nasucha, "An PC-based Airborne SAR Baseband System," Innovative Microwave Remote Sensing, 2P1, Progress in Electromagnetics Research Symposiums (PIERS 2018), 1-4 August 2018, Toyama.

J. T. S. Sumantyo, M. Y. Chua, C. E. Santosa, G. F. Panggabean, K. Tsushima, T. Watanabe, Karna Sasmita, A. Mardiyanto, F. D. Sri Sumantyo, E. T. Rahardjo, G. Wibisono, E. Supartono, S. Gao, <u>P. P. Sitompul</u>, M. Nasucha, F. Kurniawan, A. Awaludin, B. Purbantoro, Ya Qi Ji, and N. Imura, "Hinotori-C: A Full Polarimetric C Band Airborne Circularly Polarized Synthetic Aperture Radar for Disaster Monitoring," SC5: SAR Imaging and Applications, Progress in Electromagnetics Research Symposiums (PIERS 2018), 1-4 August 2018, Toyama.

<u>Peberlin Parulian Sitompul</u>, Josaphat Tetuko Sri Sumantyo "Development of Nanosatellite for Ionospheric Measurement for Earthquake Prediction," Japan Geoscience Union Meeting (JPGU) 2019, Human & Nature, and Environmental Solutions, HGG01-P06, 26 May 2019, Makuhari, Japan.

Joko Widodo, Ayaka Takahashi, Yuta Izumi, <u>Peberlin Parulian Sitompul</u>, Husnul Kausarian, A. Munir, and Josaphat Tetuko Sri Sumantyo, "Application of Polarimetric Decomposition and Interferometry SAR Using ALOS-2 PALSAR-2 Data to Detect Potential of Burned Peat Areas," PIERS, Microwave Remote Sensing, PolSAR, and Radar Imaging 1, p.71, 18, Italy, 2019.

Peberlin Parulian Sitompul, Josaphat Tetuko Sri Sumantyo, Timbul Manik, Adi Poerwono, Farohaji Kurniawan, and Mohammad Nasucha, "Analysis of Parasitic Patch for Axial Ratio Bandwidth Enhancement in Circularly-polarized-slotted Microstrip Antenna," PIERS, Microstrip Antennas, Array Antennas, Theory and Radiation 2, 199-200, 2019, Rome, Italy.

82

Appendix 2 – Design Steps, Simulation in CST and Measurement Process.

Appendix 2 – Design Steps, Simulation in CST and Measurement Process.

CST uses many methods to solve many applications such as FIT (Finite Integration Technique) for its transient solver, FEM (Finite Element Method) for its frequency-domain solver, MoM (Method of Moment) for its integral equation solver. It also has an optical simulation tool for large structures, based on the SBR Shooting and bouncing rays method (Physical Optics), it's called a solver in their lingo.

CST has many solver modules. The time-domain solver uses the Finite Integration Technique (FIT). HFSS predominantly uses the Finite Element Method (FEM). CST Microwave Studio provides many solver modules. Moreover, besides its prominent time-domain solver primely presenting the Perfect Boundary Approximation (PBA).

Here, below are steps of design and simulation of the circularly-slotted antenna (CSA) using CST Microwave Studio.

Appendix 2 – Design Steps, Simulation in CST and Measurement Process.

1. In this step, we can choose a suitable application such as EMC/ EMI, EDA/Electronic, Charged Particle Dynamics. For antenna design, we select "MW & RF & Optical", choose "Antennas" and then click the button "Next >".
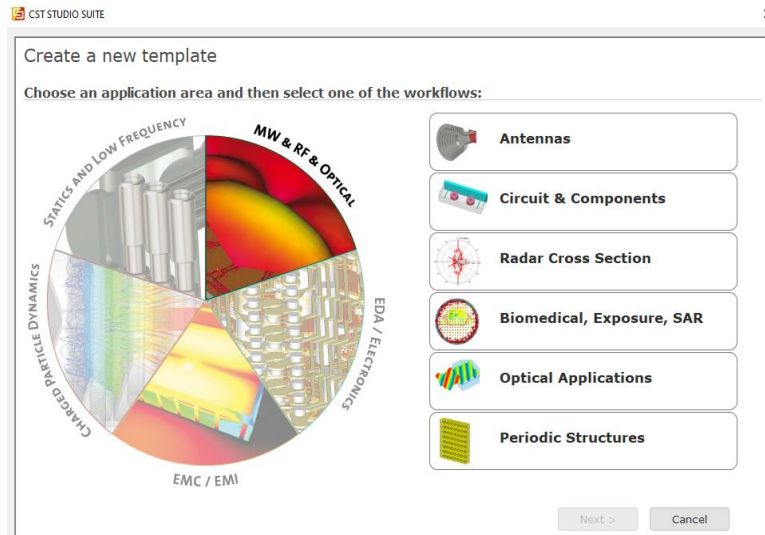
2. In this step, how to create a new template for microstrip antenna, select "Planar (Patch, Slot, etc.)" and click the button "Next >".
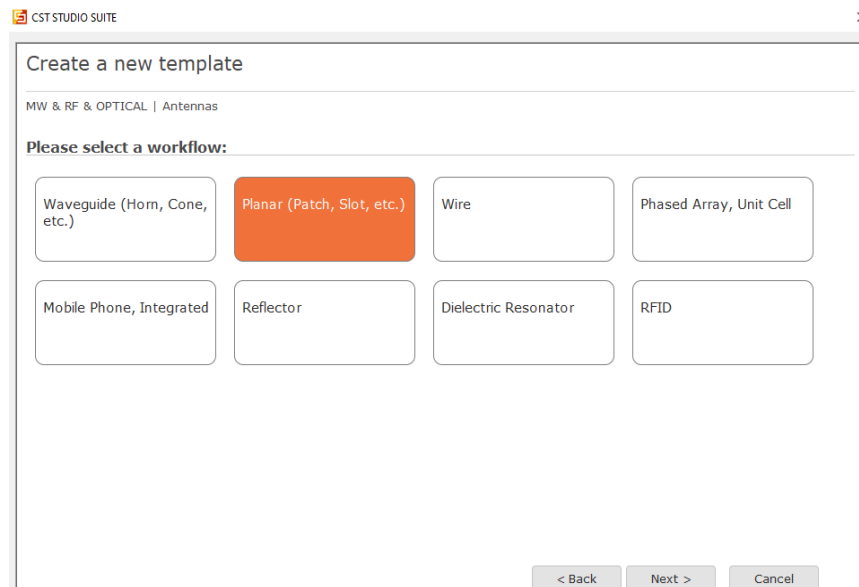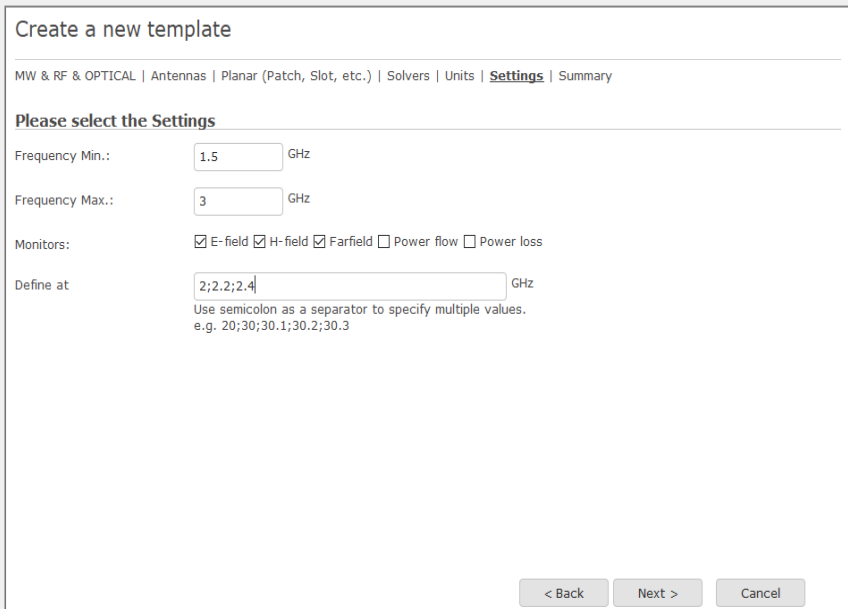
3. In this step, we can select the recommended solvers such as Time Domain, Frequency Domain, and Multilayer. For the design, choose "Time Domain" for wideband or multiband antenna and then click the button "Next >".
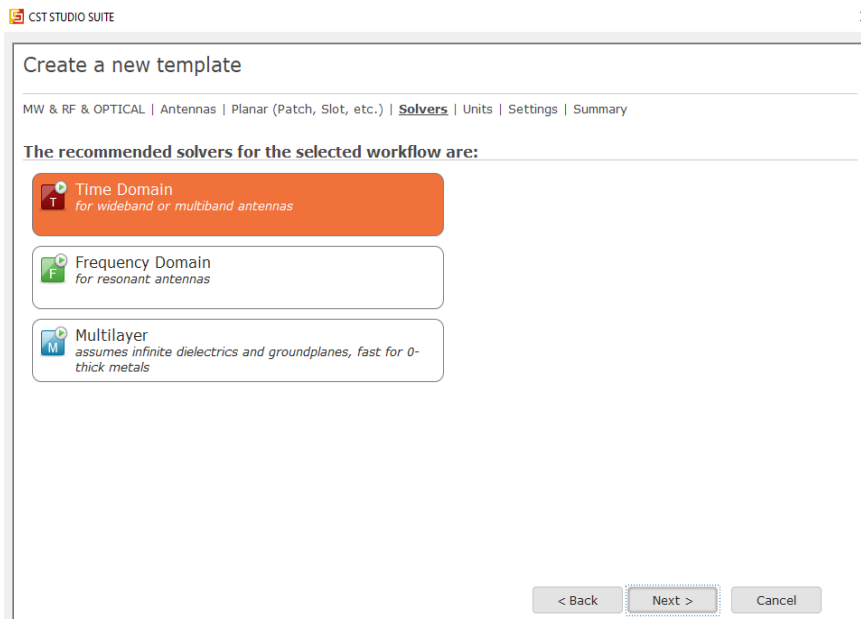
4. In this step, it shows units of the dimension, frequency, time, temperature, etc. If it is okay, click the button "Next >".
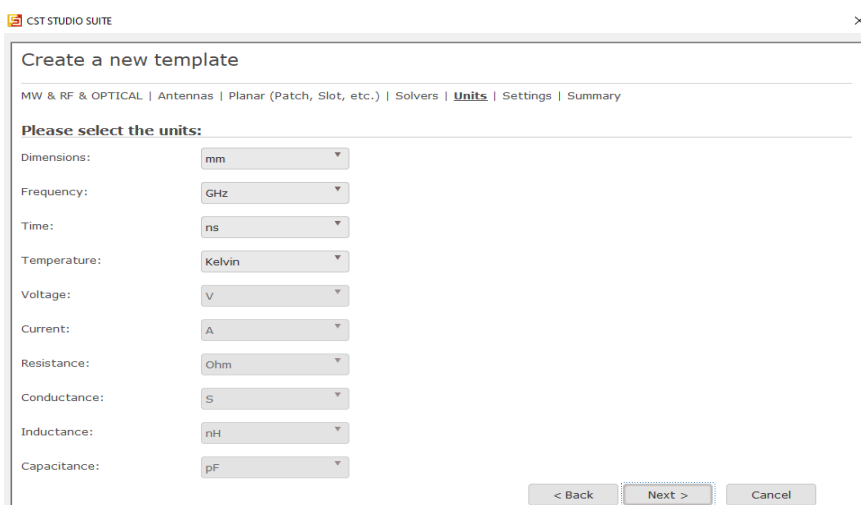
5. This step, we will choose the frequency interval for simulation. We can monitor the E field, the H field, the far-field, the power flow, the power loss, etc. We can add other parameters. We can select and define the frequencies for study. In this study, I select in frequencies of 2 GHz, 2.2 GH, and 2.4 GHz.

6. In this step, we name the template of our work, for example, "Antenna – Planar_14", then click the button "Finish".
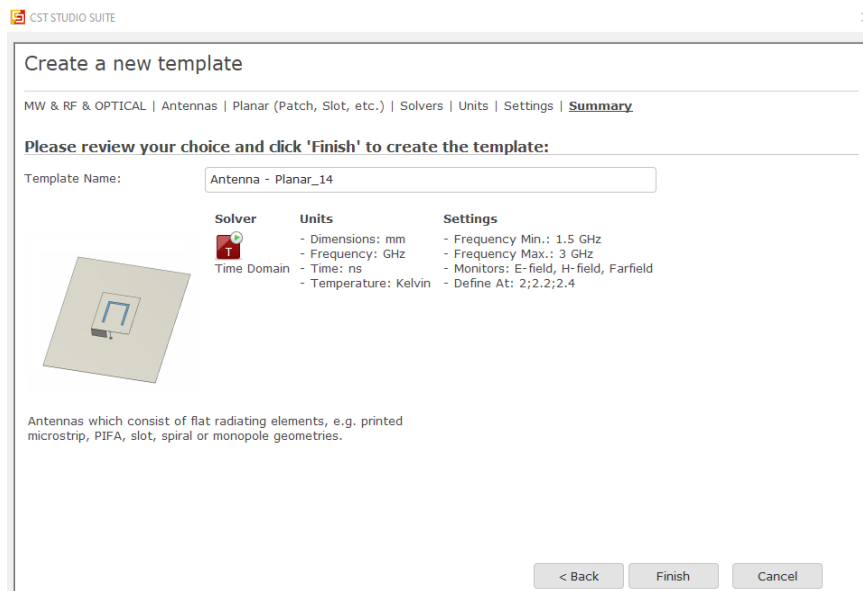
7. In this step, a template will appear on our work display, a rectangular-shaped.
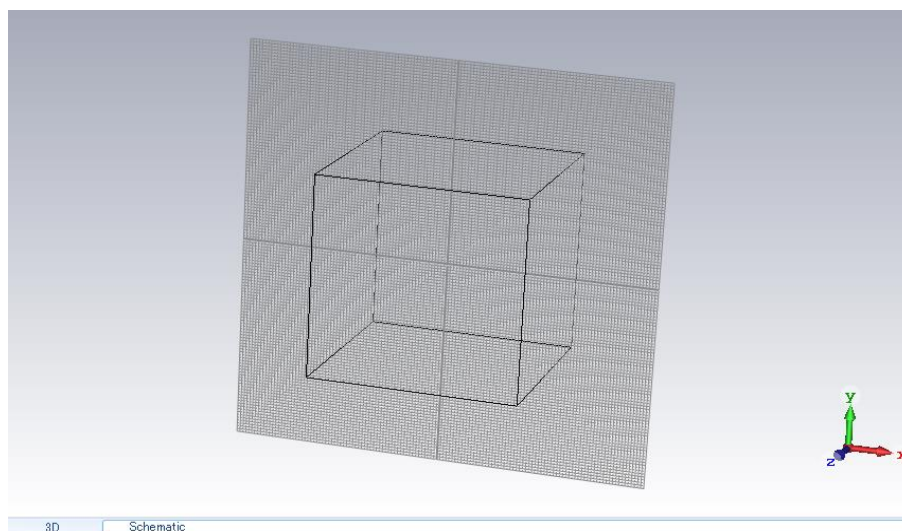
8. In this step, we create a rectangular-shaped or square-shaped based on the size of the structure (length, width, and thickness). We can also determine the material type such NPC by selecting a button Brick on Modelling Tab. This step is creating a substrate.
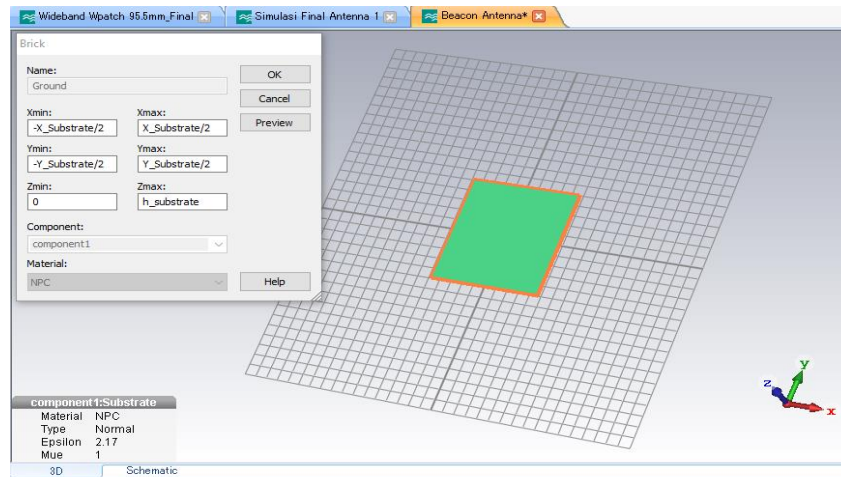
9. This step is to create a Grounded-Patch to determine the length, width, and thickness of the material. Here, the material is copper (pure), as depicted below.

Appendix 2 – Design Steps, Simulation in CST and Measurement Process.
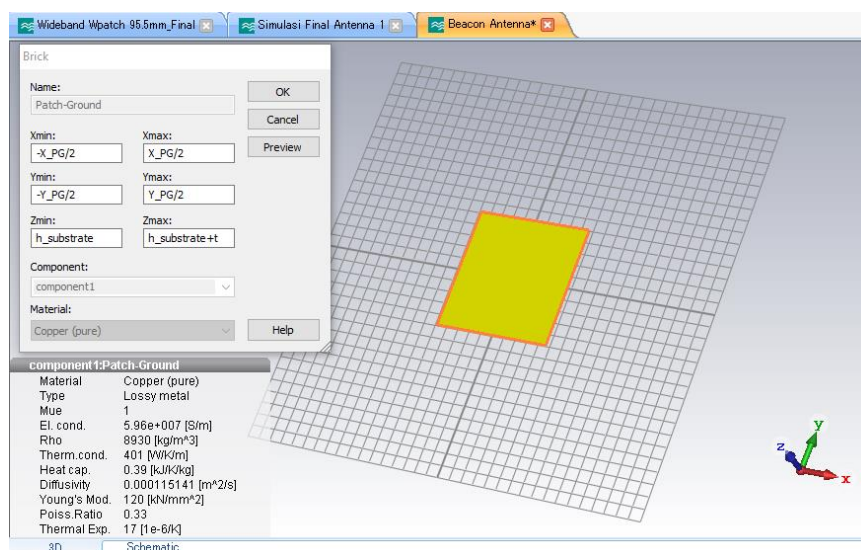
10. This step is to create a Feeding line and to determine the length, width, and thickness of the material. Here, the material is copper (pure), as depicted below.
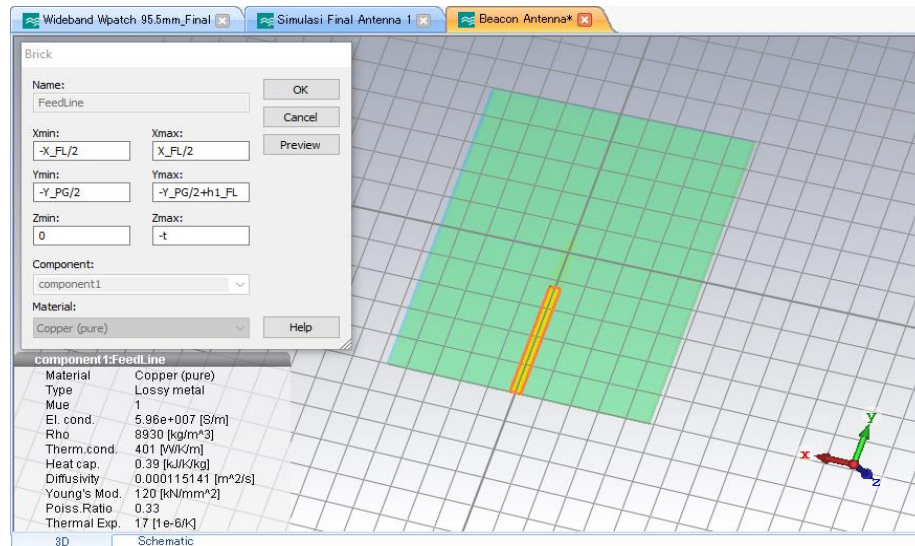
11. Creating a Circular-shaped Slot and determining length, width, and thickness of the material. Here, the material is a vacuum, as depicted below.
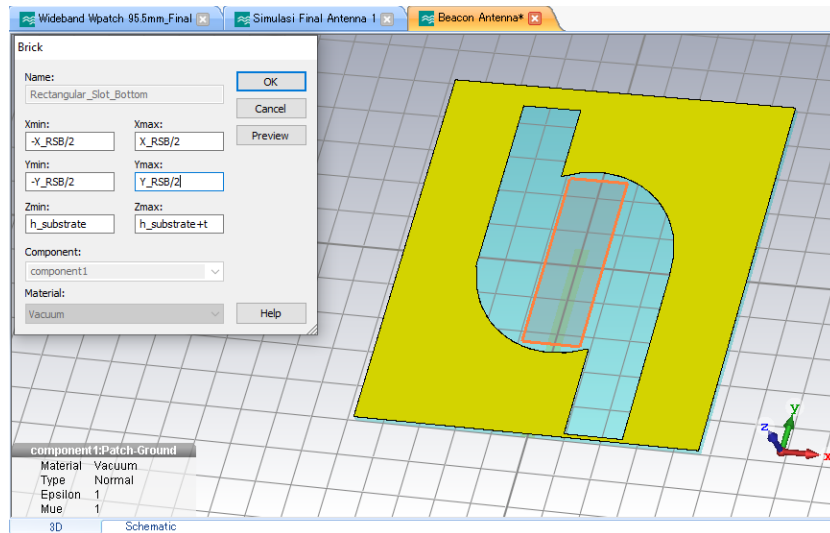
Appendix 2 – Design Steps, Simulation in CST and Measurement Process.
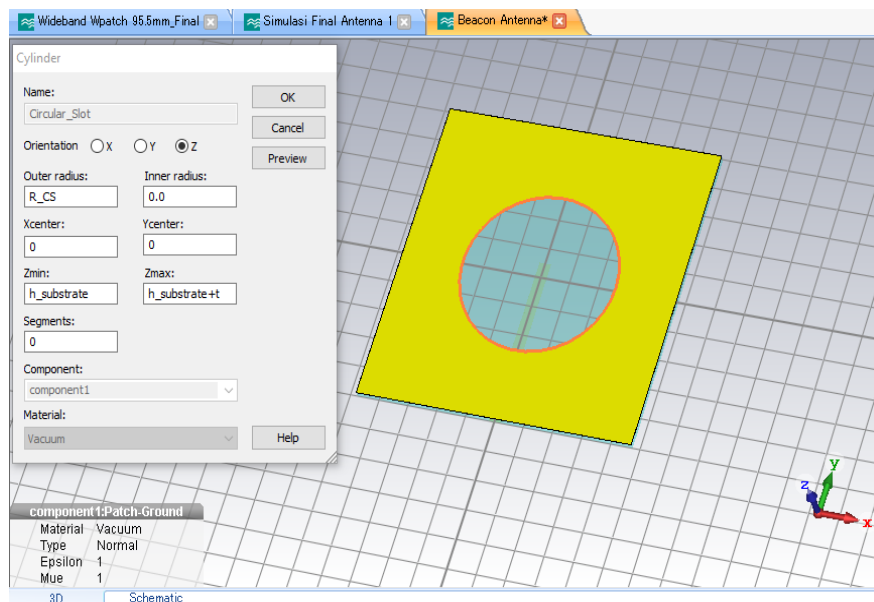
12. Creating a rectangular-shaped Slot on the bottom side, determining the length, width, and thickness of the material. Here, the material is a vacuum, as depicted below.
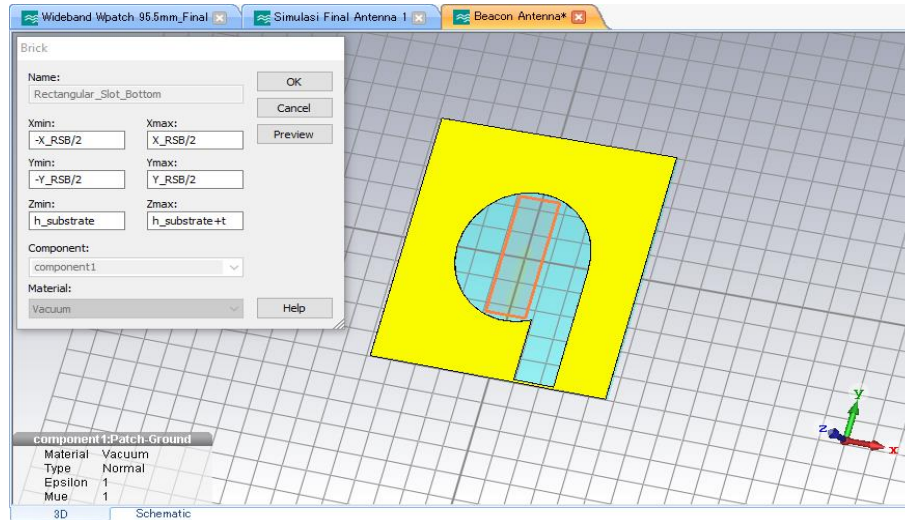
13. Creating a shifted Rectangular Slot on the bottom side, determining the length, width, and thickness of the material. Here, the material is a vacuum, as depicted below.

90

Appendix 2 – Design Steps, Simulation in CST and Measurement Process.
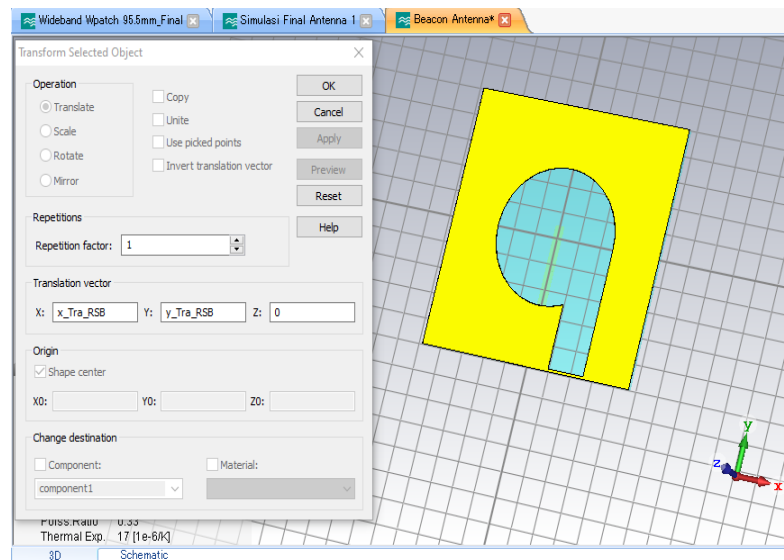
14. Creating a Rectangular Slot in the center. Determining the length, width, and thickness of the material. Here, the material is a vacuum, as depicted below.


15. Translating a Rectangular-shaped Slot on the center to the upside. Determining the length, width, and thickness of the material.
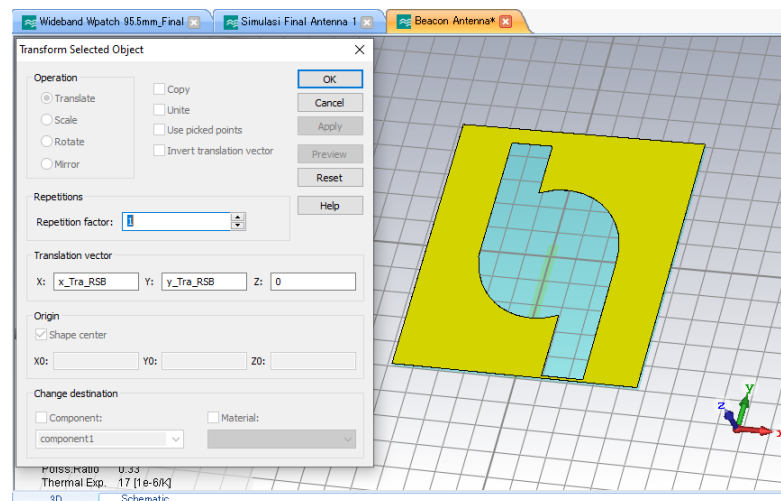
16. Shifting a feeding line to the left side. Determining the length of shifting as depicted below
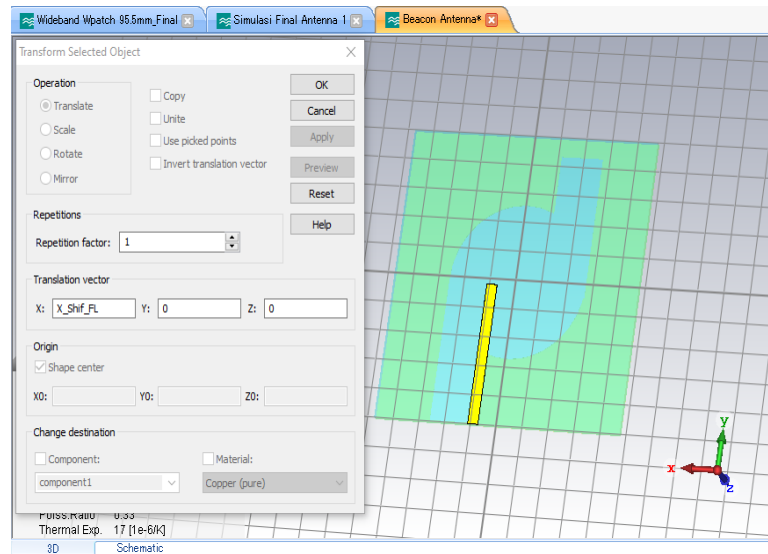
17. Changing the feeding line width on the upside for impedance tuning.

92

Appendix 2 – Design Steps, Simulation in CST and Measurement Process.
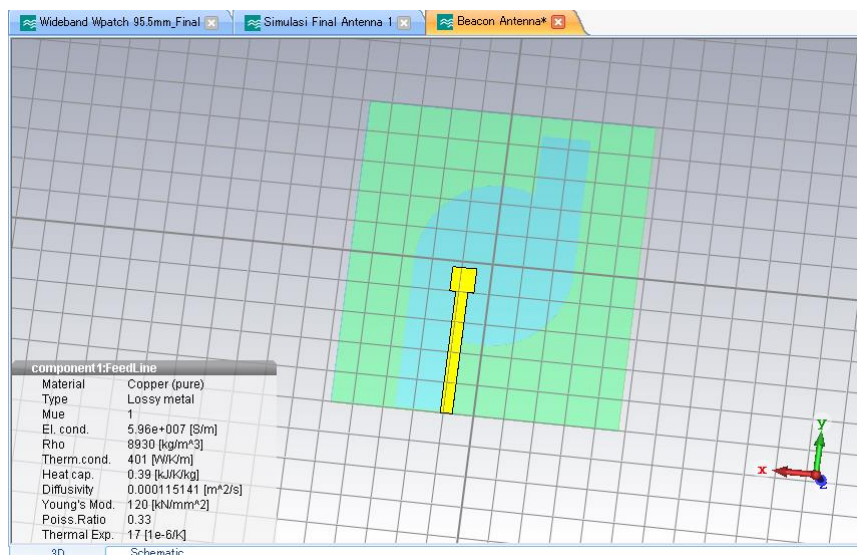
18. Creating an additional parasitic patch, on a circular-shaped slot. Determining length, width, and thickness, the material, and position of the parasitic. Here, the material is copper, as depicted below.
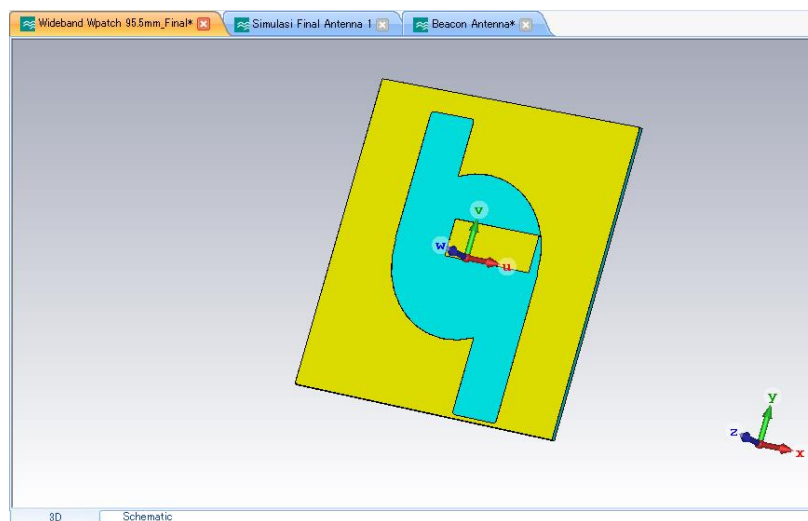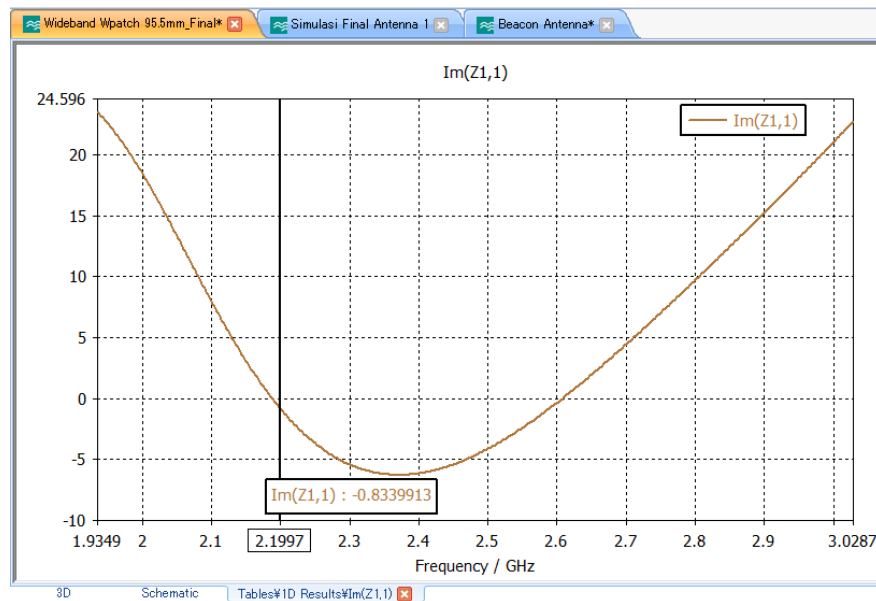

19. This step shows the simulation result of S_{11} (the Reflection coefficient) in the frequency of 2.19 GHz.

Appendix 2 – Design Steps, Simulation in CST and Measurement Process.
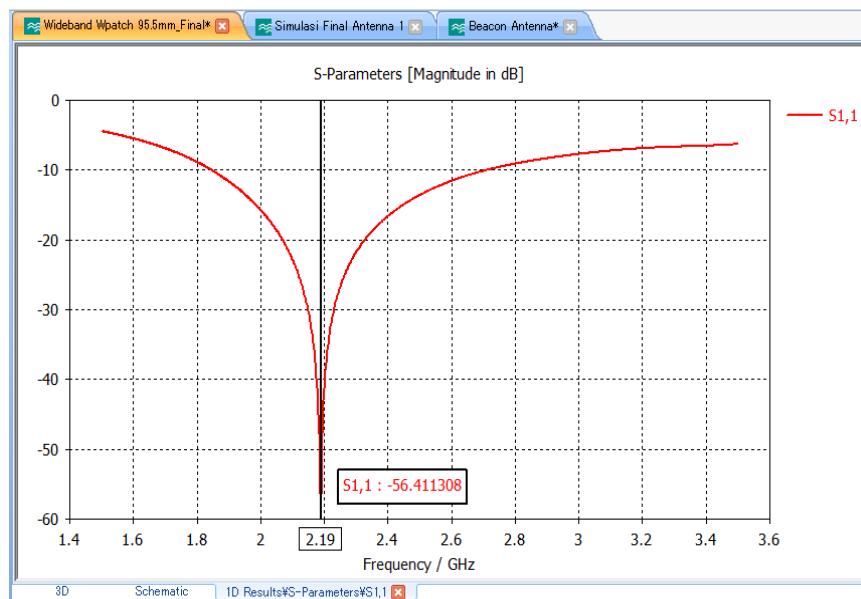
20. This step shows the simulation result of real impedance (R, in ohm). The real impedance is 55.8 ohms at frequency 2.2 GHz
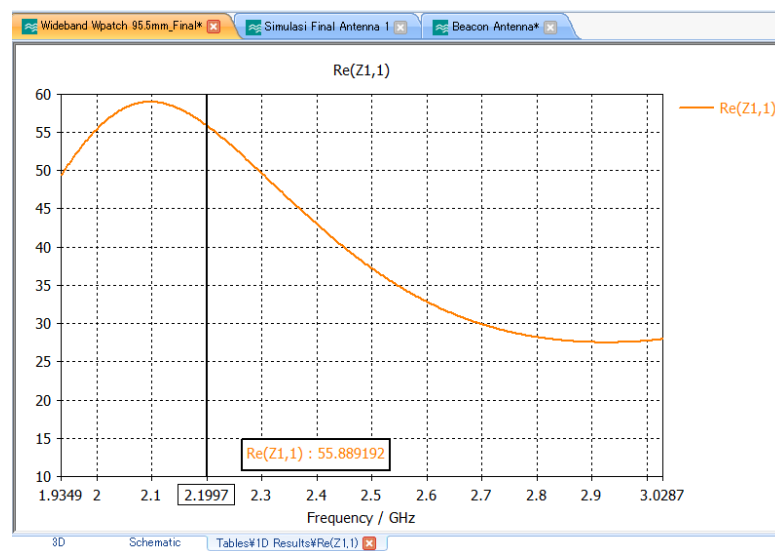

21. This shows the simulation result of the reactance of impedance (X, in ohm). The reactance is – 0.83 ohms at frequency 2.199 GHz

Appendix 2 – Design Steps, Simulation in CST and Measurement Process.

22. This one shows the simulation result of the Axial Ratio (ARBW, in dB). We can see that the 3 dB ARBW is from 2.15 GHz – 3.25 GHz.

95

Appendix 2 – Design Steps, Simulation in CST and Measurement Process.
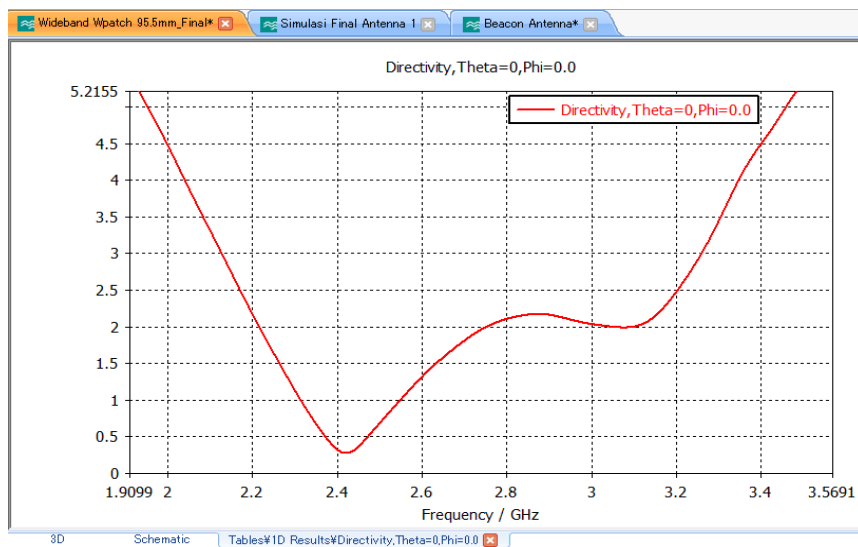
Steps for antenna fabrication consist of 7 steps :

- Design/Layout Preparation

  After antenna design has completed in CST, the design is printed in paper or tracing paper. The white color is copper, and the black color is slotted, as shown figure below.
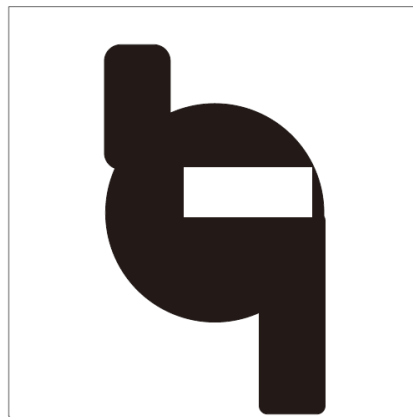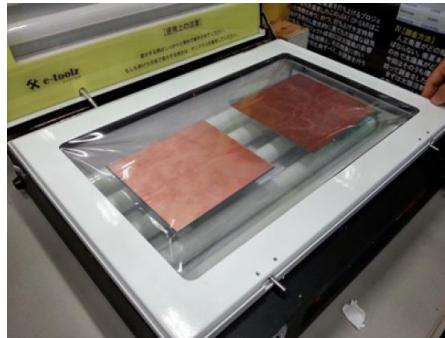

- Lamination Process.

  The lamination process is to attach the photosensitive film on the patch.

96

Appendix 2 – Design Steps, Simulation in CST and Measurement Process.
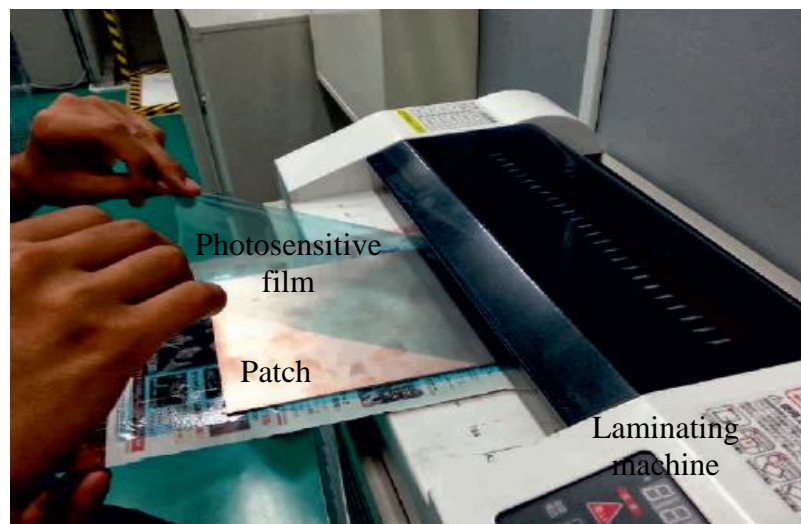
- Ultra Violet (UV) Exposure

    The UV exposure is to print the designed antenna on the Patch and
    result after the UV process, as shown on the figure below.

- Development of Antenna
- Etching
- Remove Lamination
- Cleanup

Appendix 3 – Finite Integration Technique (FIT) in CST

Steps of Maxwell Equations for cubic grids in CST.

$$\oint_{\partial s} E \, dl = -\iint_s \frac{\partial B}{\partial t} \, dS \qquad \text{[A.1]}$$

$$\iint_{\partial V} D \, dS = \iiint_V \rho \, dV \qquad \text{[A.2]}$$

$$\oint_{\partial s} H \, dl = -\iint_s \left(\frac{\partial D}{\partial t} + J\right) dS \qquad \text{[A.3]}$$

$$\iint_{\partial V} B \, dS = 0 \qquad \text{[A.4]}$$

Equation A.1, A.2, A.3, and A.4 are Maxwell equations in integral forms for the electric field, electric density, magnetic field and magnetic density.

For the simulation in FIT, a structure is divided into grids, as shown below Figure A.1.
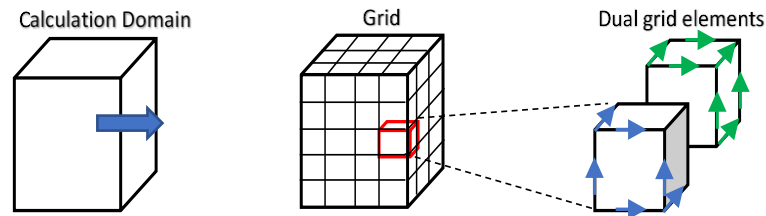

Figure A.1 Steps of Maxwell equation for a single grid in FIT

In a single grid, as shown below, consist of an electric field (*e*) and magnetic density (*b*) in a normal plane.
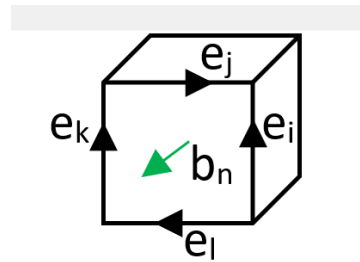

Figure A.2 Electric field and magnetic density in a single grid for FIT

Maxwell equation in a normal plane of a single grid as shown in the equation below.

$$e_i - e_j - e_k - e_l = -\frac{\partial}{\partial t} b_n \qquad \text{[A.5]}$$

$$\begin{bmatrix} 1 & -1 & -1 & -1 \end{bmatrix} \begin{bmatrix} e_i \\ e_j \\ e_k \\ e_l \end{bmatrix} = -\frac{d}{dt} [b_n] \qquad \text{[A.6]}$$

$$C\,e = -\frac{d}{dt}\,b \qquad \text{[A.7]}$$

Equation A.5, A.6, and A.7 are a step of the Maxwell equation in a single grid for Equation A.1. The same process can be done to solve other equations A.2, A.3 and A.4.

Maxwell equation in a grid is summarized as equation below Equation A.7, A.8, A.9 and A.10.

$$C\,e = -\frac{d}{dt}\,b \qquad\qquad\qquad [\text{A.7}]$$

$$S d = q \qquad\qquad\qquad [\text{A.8}]$$

$$C\,h = \frac{d}{dt}\,d + j \qquad\qquad\qquad [\text{A.9}]$$

$$S b = 0 \qquad\qquad\qquad [\text{A.10}]$$